CM² MAGAZINE

第 49 期

南方科技大学海洋磁学中心主编

创刊词

海洋是生命的摇篮，是文明的纽带。地球上最早的生命诞生于海洋，海洋里的生命最终进化成了人类，人类的文化融合又通过海洋得以实现。人因海而兴。

人类对海洋的探索从未停止。从远古时代美丽的神话传说，到麦哲伦的全球航行，再到现代对大洋的科学钻探计划，海洋逐渐从人类敬畏崇拜幻想的精神寄托演变成可以开发利用与科学研究的客观存在。其中，上个世纪与太空探索同步发展的大洋科学钻探计划将人类对海洋的认知推向了崭新的纬度：深海（deep sea）与深时（deep time）。大洋钻探计划让人类知道，奔流不息的大海之下，埋藏的却是亿万年的地球历史。它们记录了地球板块的运动，从而使板块构造学说得到证实；它们记录了地球环境的演变，从而让古海洋学方兴未艾。

在探索海洋的悠久历史中，从大航海时代的导航，到大洋钻探计划中不可或缺的磁性地层学，磁学发挥了不可替代的作用。这不是偶然，因为从微观到宏观，磁性是最基本的物理属性之一，可以说，万物皆有磁性。基于课题组的学科背景和对海洋的理解，我们对海洋的探索以磁学为主要手段，海洋磁学中心因此而生。

海洋磁学中心，简称 CM^2，一为其全名“Centre for Marine Magnetism”的缩写，另者恰与爱因斯坦著名的质能方程 $E = MC^2$ 对称，借以表达我们对科学巨匠的敬仰和对科学的不懈追求。

然而科学从来不是单打独斗的产物。我们以磁学为研究海洋的主攻利器，但绝不仅限于磁学。凡与磁学相关的领域均是我们关注的重点。为了跟踪反映国内外地球科学特别是与磁学有关的地球科学领域的最新研究进展，海洋磁学中心特地主办 CM^2 Magazine，以期与各位地球科学工作者相互交流学习、合作共进！

“海洋孕育了生命，联通了世界，促进了发展”。 21 世纪是海洋科学的时代，由陆向海，让我们携手迈进中国海洋科学的黄金时代

目 录

研究进展

林志勇等，Geology：海底沉积物中发现新型自生磁铁矿

近日，国际地学权威期刊《Geology》刊登了中山大学孙晓明教授团队林志勇博士联合国际多个科研单位的最新研究成果，报道了产于海底沉积物甲烷带中的自生磁铁矿，该发现不仅改变了人们对沉积物磁铁矿来源的传统认识，也为揭示深部沉积物微生物铁还原作用机制提供了重要线索。

保存在海洋沉积物中的磁学信号是研究地球构造演化、磁场变化和环境演变的重要工具。陆地来源的磁性铁氧化物（如磁铁矿、钒钛磁铁矿）是沉积物磁信号的重要来源。近年来科学家发现，生物成因的纳米自生磁铁矿是沉积剩磁的另一个重要载体。目前研究认为这些生物成因磁铁矿主要有两种形成途径：一是来源于趋磁细菌 （magnetotactic bacteria) 胞内合成的磁小体化石，二是通过异化铁还原细菌（dissimilatory iron-reducing bacteria）胞外合成的超细磁铁矿（Roberts, 2015）。目前人们对这两种类型磁铁矿的特征均有了一定的认识，比如磁小体化石通常有着较明确的尺寸、结构和形貌特征，而异化铁还原细菌胞外磁铁矿则尺寸更小、结晶程度更差。通常而言，大陆边缘沉积物中的有机物或甲烷含量丰富，硫酸盐还原作用较强烈，沉积物中多出现硫化（含硫化氢）现象（Jørgensen, 1982; Boetius et al., 2000），而硫化氢的存在使得沉积物中的磁铁矿难以得到良好保存。研究发现，位于海底沉积物中硫酸盐-甲烷转换界面（SMTZ）的磁化率会普遍出现低异常，这是由于该界面的硫酸盐驱动-甲烷厌氧氧化过程较为强烈，该过程释放的大量硫化氢会导致沉积物中磁铁矿等发生还原溶解（Riedinger et al., 2005; März et al., 2008; Roberts, 2015）。

在该研究中，林志勇等在对南海北部冷泉区一根长达 230 米的沉积钻孔 GMGS2-16 进行磁化率分析时，他们发现该钻孔深部出现的多个 SMTZ 界面（Lin et al., 2018）的磁化率并未出现低值，相反均出现异常高值（图 3A），这让人感到十分困惑。在进一步综合采用多种分析手段(FORC 一阶反转曲线、X 射线衍射、扫描电子显微镜、透射电子显微镜等)研究之后，他们发现一个令人非常惊讶的现象，在这些高磁化率层位中竟然保存着大量结晶良好、保存完整的纳米级

磁铁矿(图 4)！有趣的是，这些磁铁矿尺寸约为 200 至 800 纳米，且多以晶簇形式出现，其结晶特征和尺寸均有别于陆地来源以及通常认为的生物成因磁铁矿（磁小体和异化铁还原菌胞外磁铁矿；图 1，图 2），指示这些自生磁铁矿可能具有全新的成因！

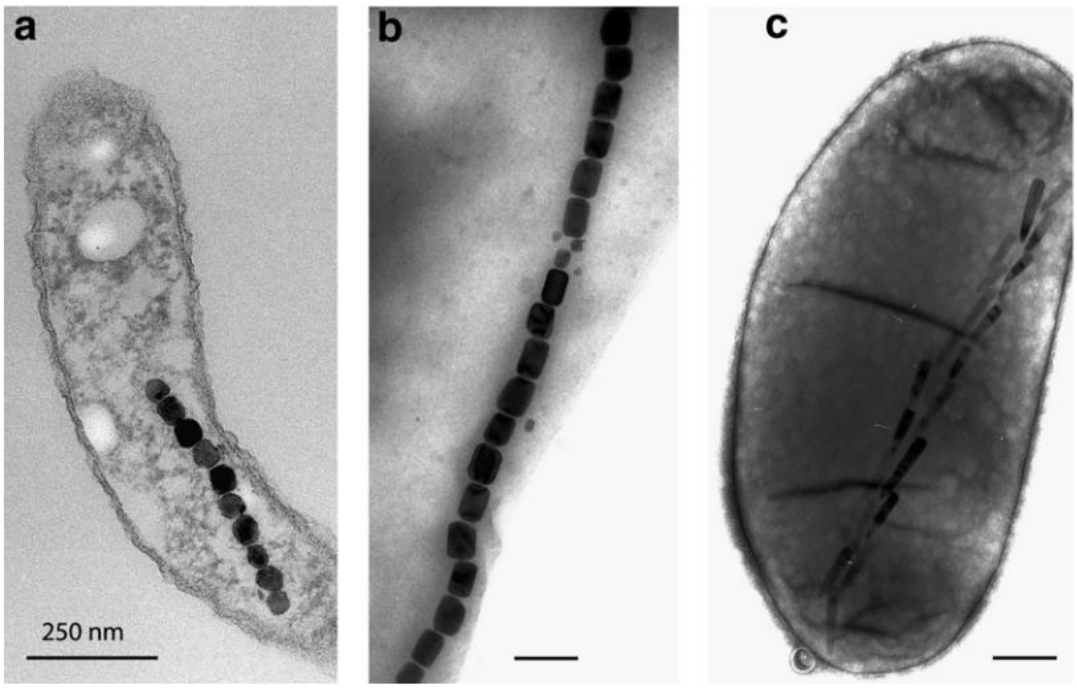

图 1. 趋磁细菌及其胞内链状排列磁小体（图自 Kopp and Kirschvink, 2008）。

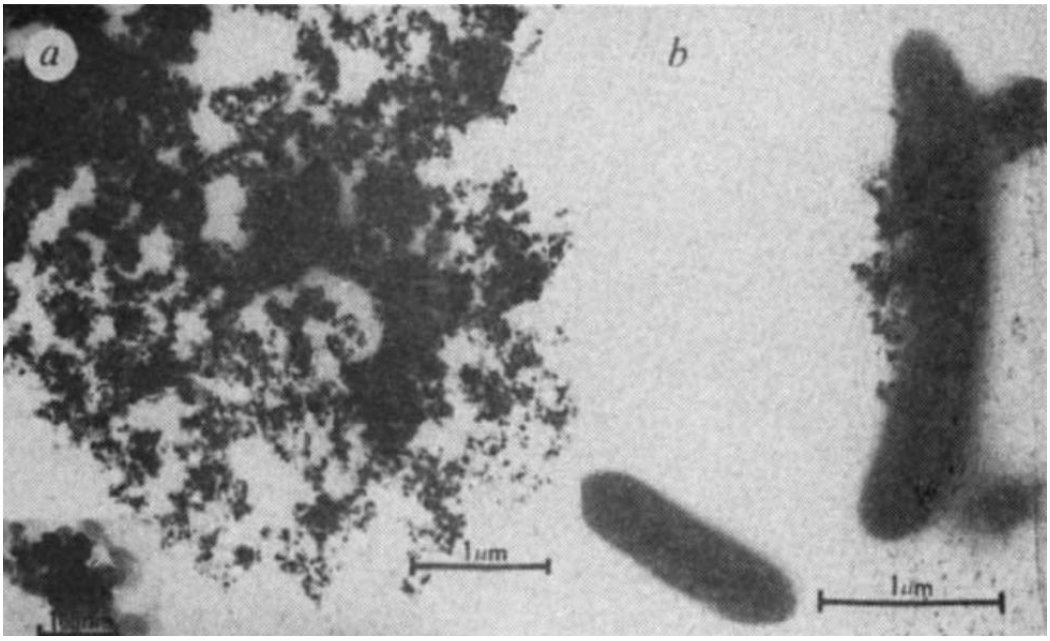

图 2. 异化铁还原细菌及其胞外不规则分布磁铁矿（图自 Lovley et al., 1987）。

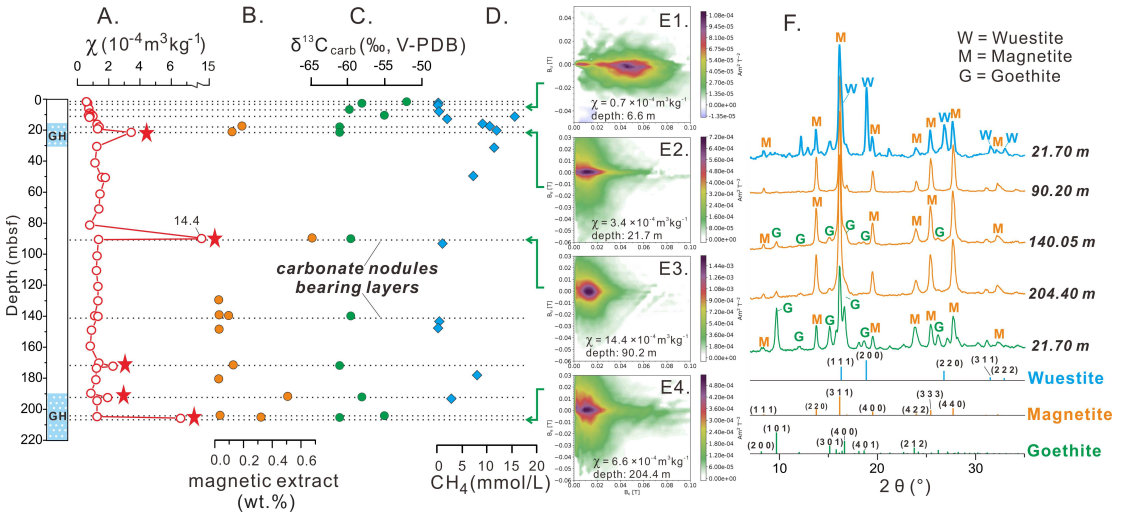

图 3. 研究钻孔 GMGS2-16 的磁学、地球化学和矿物学特征。(A)沉积物磁化率； (B) 沉积物磁性物质含量；(C) 冷泉碳酸盐结核及其碳同位素；(D)沉积物甲烷浓度；(E)沉积物一阶反转曲线（FORC 图）；(F)磁性物质 XRD 分析结果(含磁铁矿、方铁矿)。

通过结合多种生物地球化学和矿物学证据，林志勇等提出，这类磁铁矿可能是沉积物深部甲烷带微生物铁还原作用的副产物。研究钻孔 GMGS2-16 位于我国南海东北部天然气水合物赋存区，该区域高度变化的甲烷喷溢活动会导致沉积物中氧化-还原环境出现快速变化。该过程会促使 SMTZ 界面处的铁硫化物(如黄铁矿)迅速氧化，进而形成丰富的次生铁氧化物（如针铁矿和赤铁矿；图 4A-B）。这些铁氧化物一旦被快速埋藏到甲烷带，可为深部微生物铁还原作用的发生提供大量的活性铁来源，从而导致大量自生磁铁矿的形成。

沉积物甲烷带中的微生物铁还原作用是近年来生物地球化学家们热点关注的重要过程，该过程常表现出甲烷浓度的降低和铁矿物被还原二者的相互耦合，但目前人们对该过程的作用机制了解甚少（Beal et al., 2009; Egger et al., 2014；Sivan et al., 2016）。虽然甲烷带微生物铁还原作用在多种海洋和淡水沉积环境中已有诸多报道，但目前尚未有关于该过程形成自生磁铁矿的研究。该研究首次鉴定出沉积物甲烷带中微生物铁还原作用相关的自生磁铁矿，这一新的发现突破了我们关于海底沉积物磁铁矿来源的认识，对准确解释沉积磁学信号至关重要。同时，该发现可能会为科学家破解微生物铁还原作用机制提供新的线索，为揭示该类型磁铁矿形成途径提出挑战。

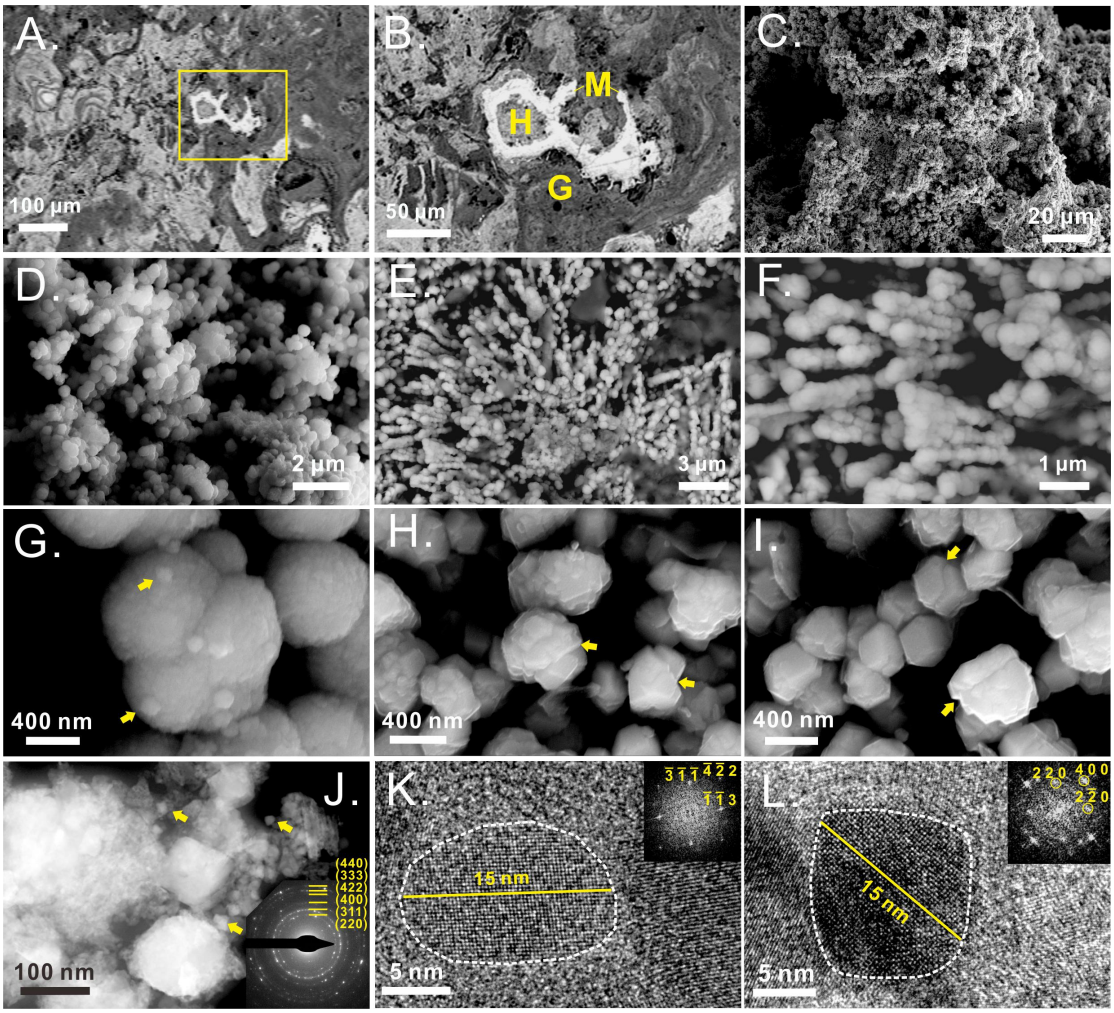

图 4. 研究钻孔 GMGS2-16 中自生纳米尺寸磁铁矿的形貌及结构。（A,B）磁铁矿（M）、赤铁矿（H）和针铁矿（G）的共生关系；(C,D)大量磁铁矿聚合体；（E,F）链状结构的磁铁矿集合体；（G-I）粒状磁铁矿及其内部结构;(J-L) 磁铁矿透射电镜（TEM)下形貌和 SAED 衍射花样。

该成果发表于《Geology》上：Lin Z Y, Sun X M, Roberts A P, et al. A novel authigenic magnetite source for sedimentary magnetization. Geology, 2020, https://doi.org/10.1130/G48069.1

作者简介：林志勇，中山大学地球科学与工程学院 2012 级“优生优培”直博生， 目前为中山大学海洋科学学院博士后，获“博士后国际交流计划派出项目”资助，现于明斯特大学进行博士后研究(为期 2 年)。目前在 Geology、GCA、Chemical Geology、Marine Geology 等期刊共发表 8 篇一作 SCI 论文。主持国家自然科学基金青年项目，国家重点研发计划子课题，博士后面上项目（一等资助）等科研项目 4 项。

磁学演绎

第 39 章　磁性矿物转化

铁离子分为二价 Fe^{2+}（Ferrous）和三价 Fe^{3+}（Ferric）。当 pH > 5 时，Fe^{2+}会被氧化成 Fe^{3+}:

$Fe^{2+} + 3H_2O \rightarrow Fe(OH)_3 + 3H^+ + e^{-1}$

$2Fe^{2+} + 4HCO_3^- + 1/2O_2 + 4H_2O \rightarrow Fe_2O_3 + 4CO_2 + 6H_2O$

$Fe_2O_3 + H_2O \rightarrow 2FeOOH$

当 Fe^{2+}从黏土矿物中析出来后，先被氧化成 Fe^{3+}，和水结合形成水铁矿（Ferrihydrite），以水铁矿为基础，后向赤铁矿和针铁矿方向转化。一般情况下，赤铁矿和针铁矿成对出现，当相对湿度较小时，赤铁矿更容易形成，当升高温度时，赤铁矿也会相对针铁矿更容易出现。如果水铁矿中的 Fe^{3+}被 Al^{3+}替代，那么 Al-Ferrihydrite 不容易形成针铁矿。这说明，赤铁矿更容易在比较干燥、高温以及晶格中有杂质的情况下形成。

如何来理解赤铁矿和针铁矿的这种竞争关系？

针铁矿的形成需要水铁矿先溶解，然后再结晶。而赤铁矿则需要水铁矿先聚集，然后晶格发生拓扑形成赤铁矿。

水铁矿粒径很小，一般在几个到十几个 nm。所以所有能促进水铁矿溶解的环境条件都促进针铁矿形成，所有能促进水铁矿聚集的条件则促进赤铁矿的形成。

我们先来看温度，温度升高，水铁矿的溶解率降低，更适合谁的生成？显然溶解率降低，针铁矿就不容易形成了，只能是赤铁矿占主导。

我们可以根据赤铁矿和针铁矿的含量，用反推法来看看水铁矿的溶解速率。pH 对针铁矿和赤铁矿的形成非常重要。pH = 7-8，温度 = 4-90 °C，赤铁矿占主导。pH = 12-14 时，针铁矿是唯一的产出物。

我们的问题是：水铁矿的溶解率在什么 pH 值附近最高？

显然，在 pH = 12-14 时，水铁矿的溶解速率最高，所以针铁矿最容易形成。

如果溶液中还有很多其他的有机质，比如 P，会对反应造成什么样的影响？这种杂质会吸附在水铁矿表面，既可以阻止水铁矿溶解，让针铁矿不容易产出。同时也可以阻止水铁矿凝聚，从而在赤铁矿也不容易转化成。

如果存在 Al^{3+}，Al^{3+}会和 Fe^{3+}发生竞争关系，不容易让针铁矿结晶。但是含铝赤铁矿还是能够聚集的，所以更容易产生含铝赤铁矿。

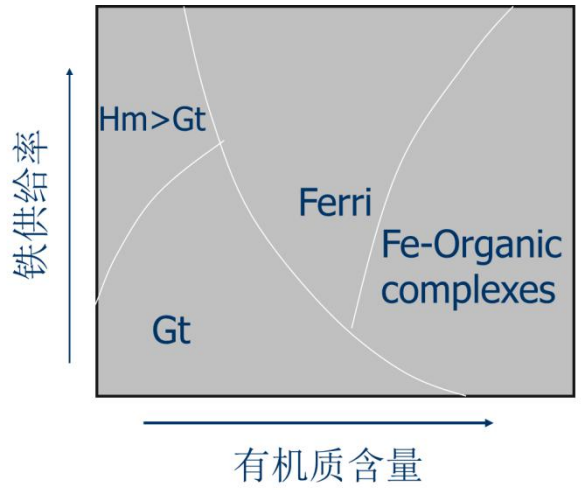

图 1 水铁矿转换与铁供给率和有机质含量的关系图

我来看看铁供给率的影响，当 Fe 含量很高时，水铁矿浓度会变大，更容易发生聚集所以赤铁矿更容易形成。反之，当铁含量很低，水铁矿的含量也会相应低，这时候更容易形成针铁矿。

当有机质含量比较高时，赤铁矿和针铁矿都不容易形成，从而保持稳定的水铁矿状态。当有机质含量更高时，铁会和有机质形成一种有机配合物。所以在自然界，要想去找水铁矿，必须去找有机质含量比较高的土壤。

我们来总结一下赤铁矿和针铁矿的形成环境。赤铁矿主要形成环境：温度高（低纬度、低海拔、或者高温环境）、干燥、土壤下部（有机质含量低）、以及铁含量高的母岩（铁供给率高，水铁矿含量高，容易聚集）。

针铁矿的形成环境：温度低（高纬度、高海拔、低温）、潮湿、土壤上部（有机质含量偏高、铁含量地的母岩、高铝）。

我们观察一个土壤剖面，在其顶部有机质含量高，所以更容易形成针铁矿。在土壤中下部，土壤的颜色会变红，这是因为形成了很过纳米级的染色赤铁矿。

磁性矿物之间，由于氧化还原环境的变化，会发生相互转化。但是，无论如何针铁矿的形成一定需要一个先溶解后结晶的过程，而赤铁矿则不需要。只要把 Fe^{2+}氧化成 Fe^{3+}，或者把晶格中的水成分析出来就可以了。

通过研磨或者加热，针铁矿晶格中的水析出，就可以形成赤铁矿。当然其中有可能会生成中间产物磁赤铁矿。

水铁矿可以转化为几乎所有的常见磁性矿物。加热直接形成赤铁矿。溶解沉淀则形成针铁矿。如果在溶解沉淀时，存在 Fe^{2+}，还可以形成磁铁矿。

在还原环境中，赤铁矿和磁赤铁矿可以转化为磁铁矿。反之，在氧化环境下，磁铁矿可以被氧化成磁赤铁矿和赤铁矿。在低温氧化状态下，大颗粒磁铁矿可以被氧化成一种核壳结构，内核是磁铁矿，而外壳是磁赤铁矿。由于核和壳之间的晶格结构不同，造成不匹配额现象，所以这种核壳结构会产生较高的矫顽力。但是已经过热处理，这种核壳结构消失，矫顽力也就会降低下来。

针铁矿受热转换为赤铁矿，转换温度随着晶型提高而升高（260→320 °C）。Al 成份增加，转换温度也升高。在转化中，阴离子格架基本不变，脱水，阳离子重新排列。3 个针铁矿 Unit cell → 1 个 Hem Unit cell。

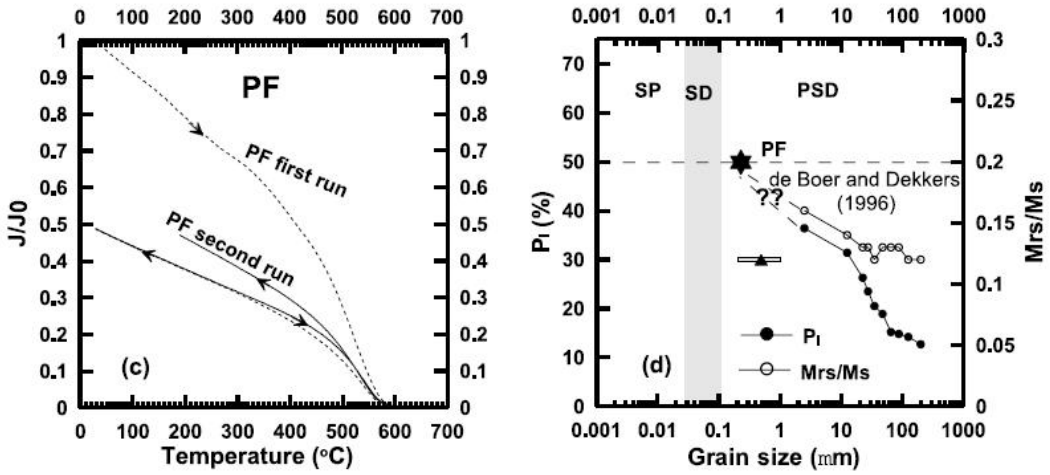

图 2 磁赤铁矿受热转化为赤铁矿

磁赤铁矿受热会转化为赤铁矿，造成磁性的大幅度降低。但是，这种转化与磁赤铁矿的粒径密切相关。磁赤铁矿颗粒越大，就越稳定。可以定义 J-T 曲线中，经过一次热处理，其饱和磁化强度会比初始值低，这就表明磁赤铁矿发生了转化，把二者的比值作转化率（P_I）。对于大颗粒磁赤铁矿，P_I 才 10%左右。在几百纳米，P_I 可以达到 50%。对中国黄土高坡古土壤中系里磁赤铁矿加热表明，其最大粒径可以达到几百纳米，所对应的 P_I 约为 50%。

文献速递

1. 通过机器学习可以识别中国黄土高原地区的源区

翻译人：仲义 zhongy@sustech.edu.cn

Lin X, Chang H, Wang K B, et al. ***Machine Learning for source identification of dust on the Chinese Loess Plateau*** *[J]. Geophysical Research Letters, 2020, 47: e2020GL088950.*

https://doi.org/10.1029/2020GL088950

摘要：中国黄土高原（CLP）风尘沉积源区仍然存在争议。本文作者应用向量和卷积神经网络的机器学习方法，利用 8 个潜在源区的表层沉积物元素组成对模型进行训练，从而通过对黄土高原（CLP）区的末次冰期黄土和当前的间冰期沉积物进行分类，确定沙尘的来源和贡献。机器模型在最后一个冰期-间冰期旋回期间成功地区分了主要的二次源，并定量估计了原生和次生源的贡献。尽管气候条件不断变化，但仍有持续的尘土来源，这一认识与 Sr-Nd 同位素和 U-Pb 年龄谱得到的认识是一致的。我们的结果表明，通过大量地球化学数据集和机器学习技术完全有能力追踪来源。

ABSTRACT: The provenance of voluminous eolian dust on the Chinese Loess Plateau (CLP) is still highly debated. Here we apply machine learning methods of support vector machine and convolutional neural network to train models using element compositions of surface sediments from eight potential source regions, accordingly, to determine the dust sources and contributions by classifying the last glacial loess and present interglacial sediments on the CLP. The trained models succeed in differentiating major secondary sources and quantitatively estimating the contributions of both primary and secondary sources at least during the last glacial-interglacial cycle. The understanding that a constant dust source despite changing climate conditions agrees with those derived from Sr-Nd isotopes and U-Pb age spectra. Our observations demonstrate that big geochemical data sets coupled with machine learning technology are fully capable of tracing sources.

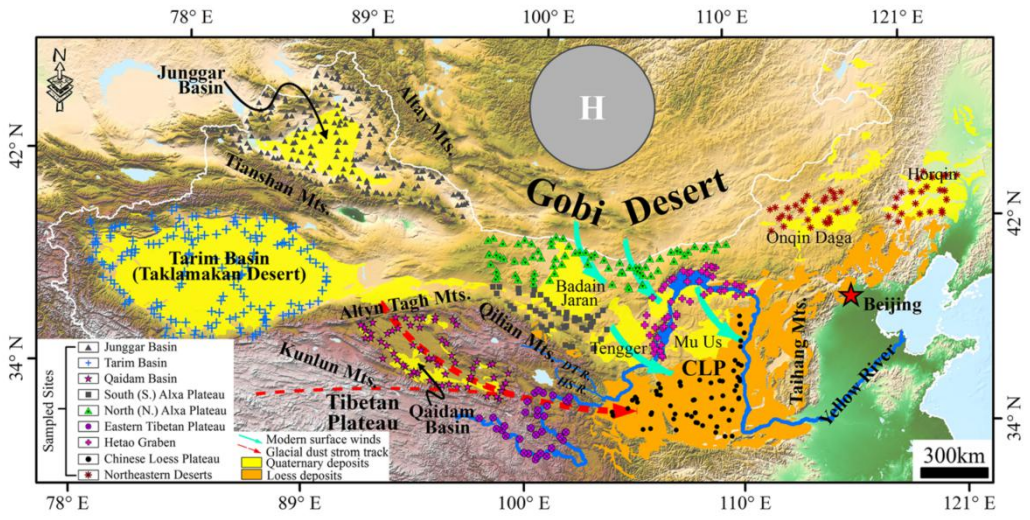

Figure 1. Map showing the shaded relief of central East Asia and the sampled sites. The continental-scale geochemical mapping covers the Chinese Loess Plateau (CLP) and eight potential source regions (PSRs). Glacial dust storm track and modern surface winds are according to Pullen et al. (2011). Circled H means high pressure over Central Asia. DT R. and HS R. are Datong River and Huangshui River, respectively.

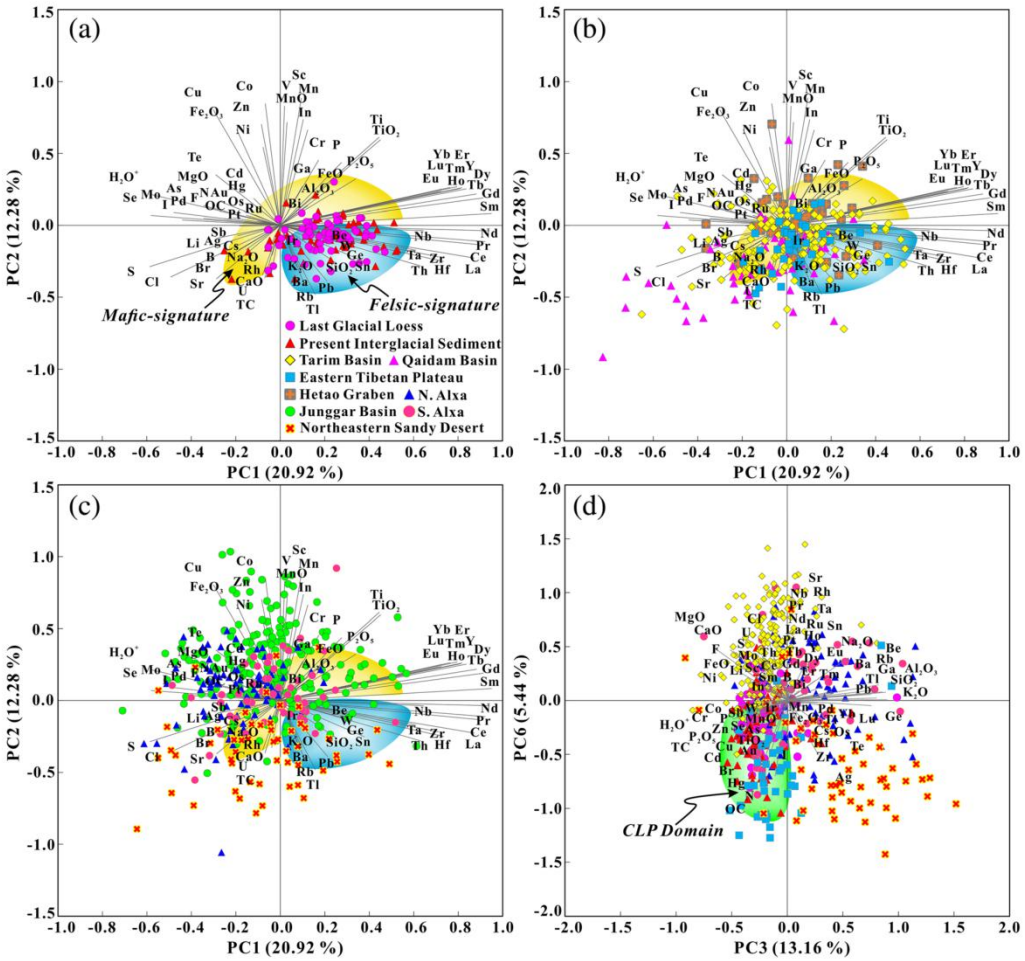

Figure 2. Compositional biplots of LGL, PIS, and PSRs. (a–c) PC1 versus PC2 and (d) PC3 versus PC6 (some of the PSRs that show similar distribution patterns with that on PC1 vs. PC2 biplot are not included to avoid serious spatial overlap). PC loadings for each element are plotted as black lines. Numbers in bracket denote the variance accounted by PCs. LGL = last glacial loess; PIS = present interglacial sediments; PSRs = potential source regions.

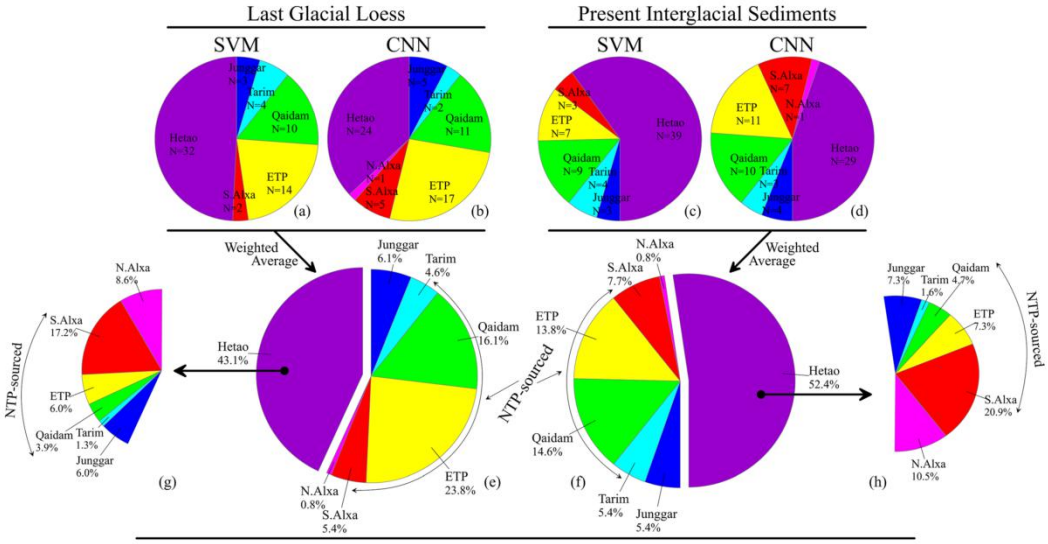

Figure 3. Pie charts showing the dust classification using support vector machine (SVM) and convolutional neural network (CNN). (a, b) The last glacial loess (LGL). (c, d) The present interglacial sediments (PIS). (e, f) The weighted average proportions of LGL and PIS in the eight potential source regions (PSRs), respectively. (g, h) The decomposition of the Hetao Graben into six other PSRs. N = number; ETP = eastern Tibetan Plateau; N. Alxa = North Alxa Plateau; S. Alxa = South Alxa Plateau; NTP = northern Tibetan Plateau consisting of the Qilian Mountain, Qaidam Basin, and eastern Tibetan Plateau.

2. 切叶蚂蚁的生物矿物盔甲

翻译人：蒋晓东 jiangxd@sustech.edu.cn

Li H J, Sun C F, Fang Y H, et al. ***Biomineral armor in leaf-cutter ants*** *[J]. Nature Communications, 2020, 11: 5792.*

https://doi.org/10.1038/s41467-020-19566-3

摘要：尽管钙质解剖学结构在动物群组中已经进化除出多样，然而昆虫中的相关结构还并不清楚，本研究报道了大多数切叶蚁工蚁的外骨骼均覆盖着高镁方解石盔甲。切叶蚁培养与试管合成实验表明工蚁成熟时上表皮催化生物矿物层形成与快速堆积，并且持续扩散到整个外表。原位纳米测试表明生物矿物使外骨骼显著变硬。在与其他蚂蚁遭遇战后具有生物矿物层外骨骼的工蚁幸存者增多，而被病原真菌侵袭时感染者较少，这表明生物矿物层具有显著的保护作用。切叶蚁中生物高镁方解石的发现，钙质生物矿物富集镁质很可能比先前认识的多。

ABSTRACT: Although calcareous anatomical structures have evolved in diverse animal groups, such structures have been unknown in insects. Here, we report the discovery of high-magnesium calcite [$CaMg(CO_3)_2$] armor overlaying the exoskeletons of major workers of the leaf-cutter ant Acromyrmex echinatior. Live-rearing and in vitro synthesis experiments indicate that the biomineral layer accumulates rapidly as ant workers mature, that the layer is continuously distributed, covering nearly the entire integument, and that the ant epicuticle catalyzes biomineral nucleation and growth. In situ nanoindentation demonstrates that the biomineral layer significantly hardens the exoskeleton. Increased survival of ant workers with biomineralized exoskeletons during aggressive encounters with other ants and reduced infection by entomopathogenic fungi demonstrate the protective role of the biomineral layer. The discovery of biogenic high-magnesium calcite in the relatively well-studied leaf-cutting ants suggests that calcareous biominerals enriched in magnesium may be more common in metazoans than previously recognized.

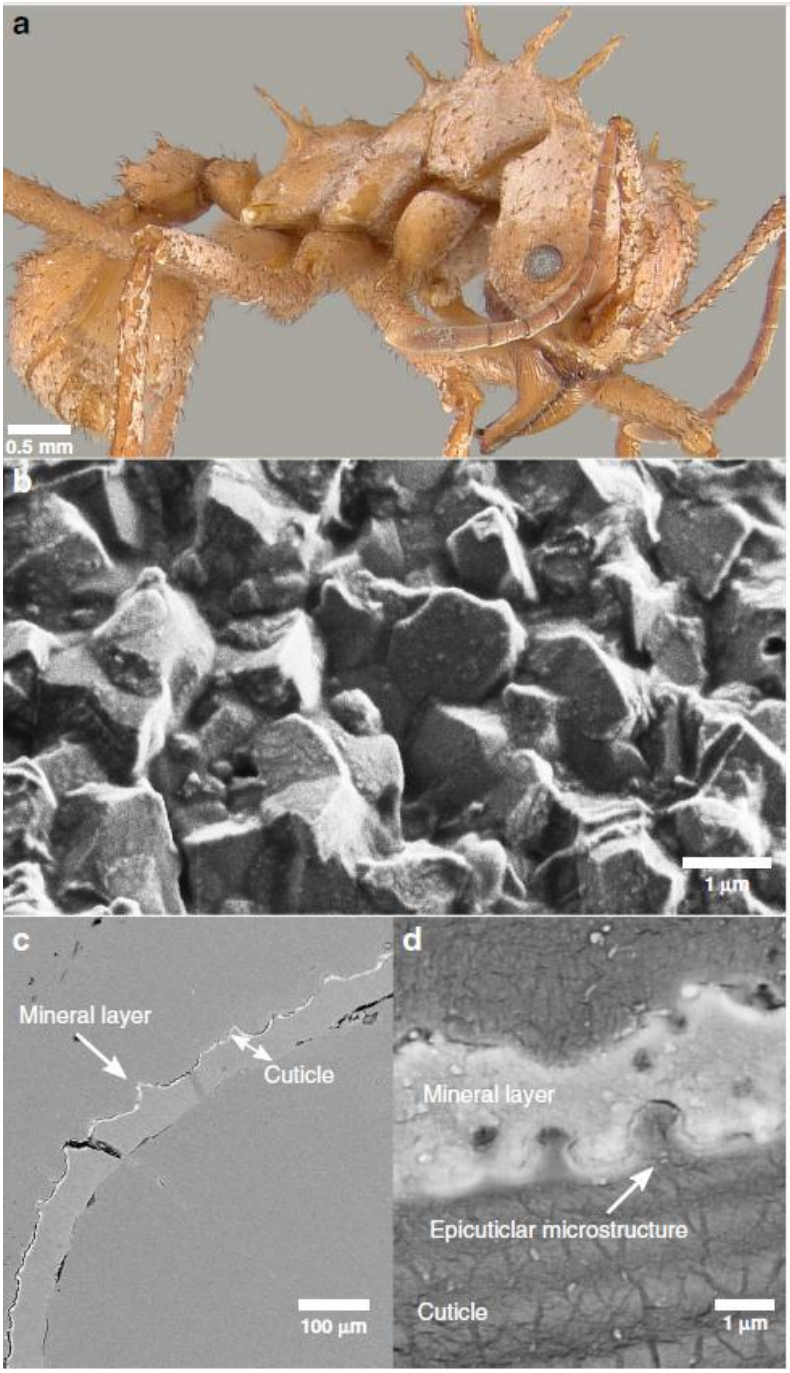

Figure 1. Morphological and structural characterization of minerals on the cuticle of Ac. echinatior. a Ac. echinatior ant with a whitish cuticular coating (Photo T.R.S.). b SEM image of ant cuticle with crystalline coating. c Backscattered electron (BSE) image of a polished cuticular cross-section of an ant. This layer is brighter than the cuticle in backscattered electron (BSE) mode scanning electron microscopy (SEM), indicating that it consists of heavier elements and is continuous, covering nearly the entire surface. d BSE image close-up of a polished cuticular cross-section of an ant.

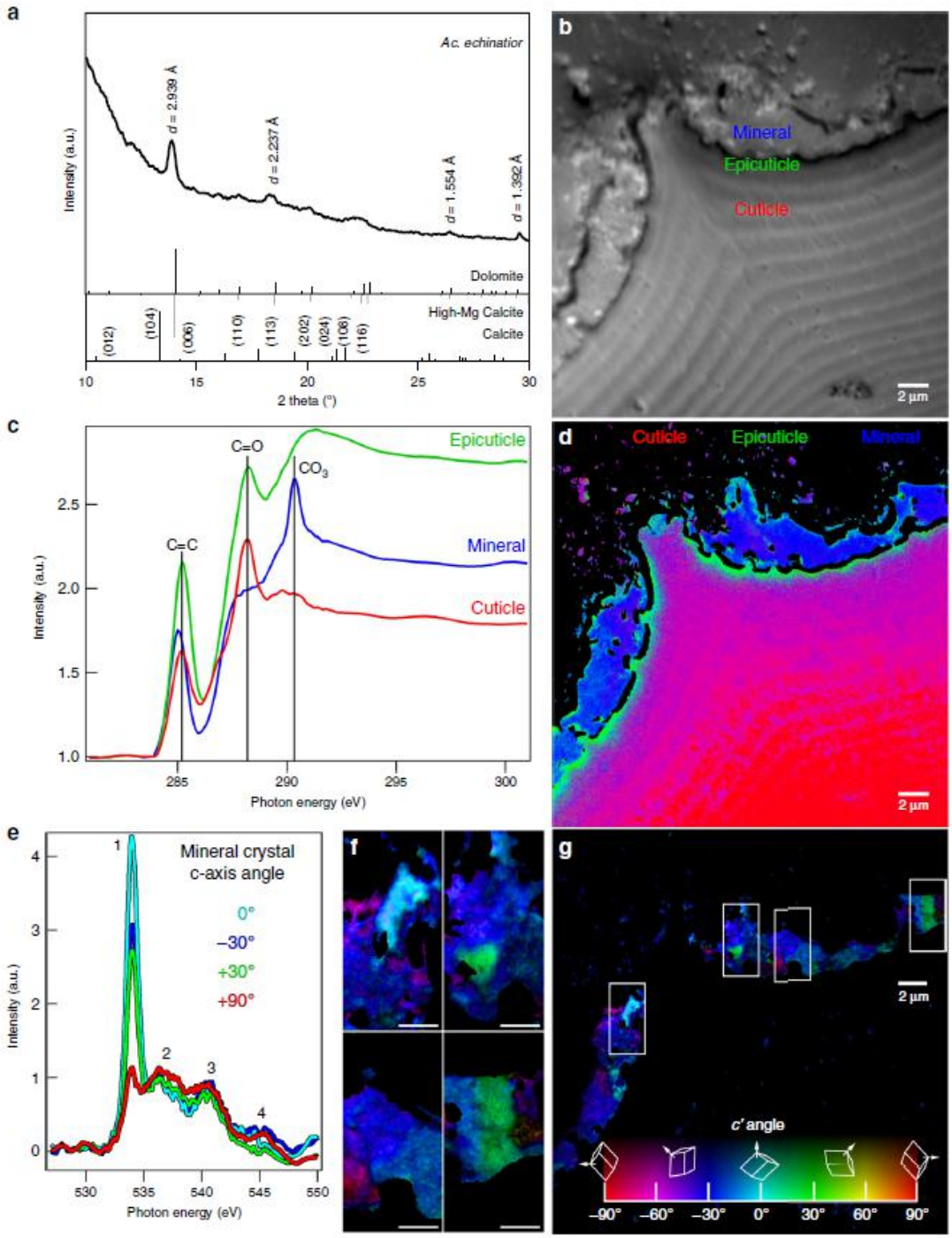

Figure 2. Chemical characterization of minerals on the cuticle of Ac. echinatior. a In situ XRD analysis identifying the cuticular crystalline layer as high-Mg calcite. b–g XANES spectroscopy and mapping with PEEM of a cuticular cross-section. b Average of PEEM images acquired across the C K-edge, showing crystalline layer tightly attached to the cuticle. Three distinct component spectra were identified in the regions labeled cuticle, epicuticle, and mineral, from the most internal part of the ant to the outer surface. c Normalized component spectra extracted from the corresponding labeled regions.

Characteristic peaks are marked, including the 285.2 eV (C=C), 288.2 eV (C = O) and 290.3 eV (carbonate) peaks. d Component map where each pixel is colored according to the chemical components it contains. Black pixels are masked areas containing epoxy or gaps. Faint carbonate components within the cuticle and epicuticle were emphasized by enhancing the blue channel 5×, thus this is a semi-quantitative map. A fully quantitative RGB component map is presented in Supplementary Fig. 21. Individual maps of each component are presented in Supplementary Fig. 22, clearly showing an increasing gradient of carbonates towards the surface in the cuticle. e O K-edge spectra extracted from the mineral crystals correspondingly colored in the Polarizationdependent Imaging Contrast (PIC) maps in f and g. f Magnified PIC maps for the regions represented by boxes in the complete PIC map in g. g PIC map quantitatively displaying the orientations of the mineral crystals' c-axes in colors. This map was acquired from the same area shown in b and d at precisely the same magnification. These are interspersed high- and low-Mg calcite, and heterogenous at the nanoscale. Biomineral crystals do not show preferred orientations but are randomly oriented. High-magnesium calcite in carbon spectra is identified by the carbonate peak at 290.3 eV, which occurs in all carbonates, amorphous, or crystalline. The O spectra in d clearly indicate crystallinity, and their line shape indicates a mixture of high-magnesium calcite and low Mg-bearing calcite.

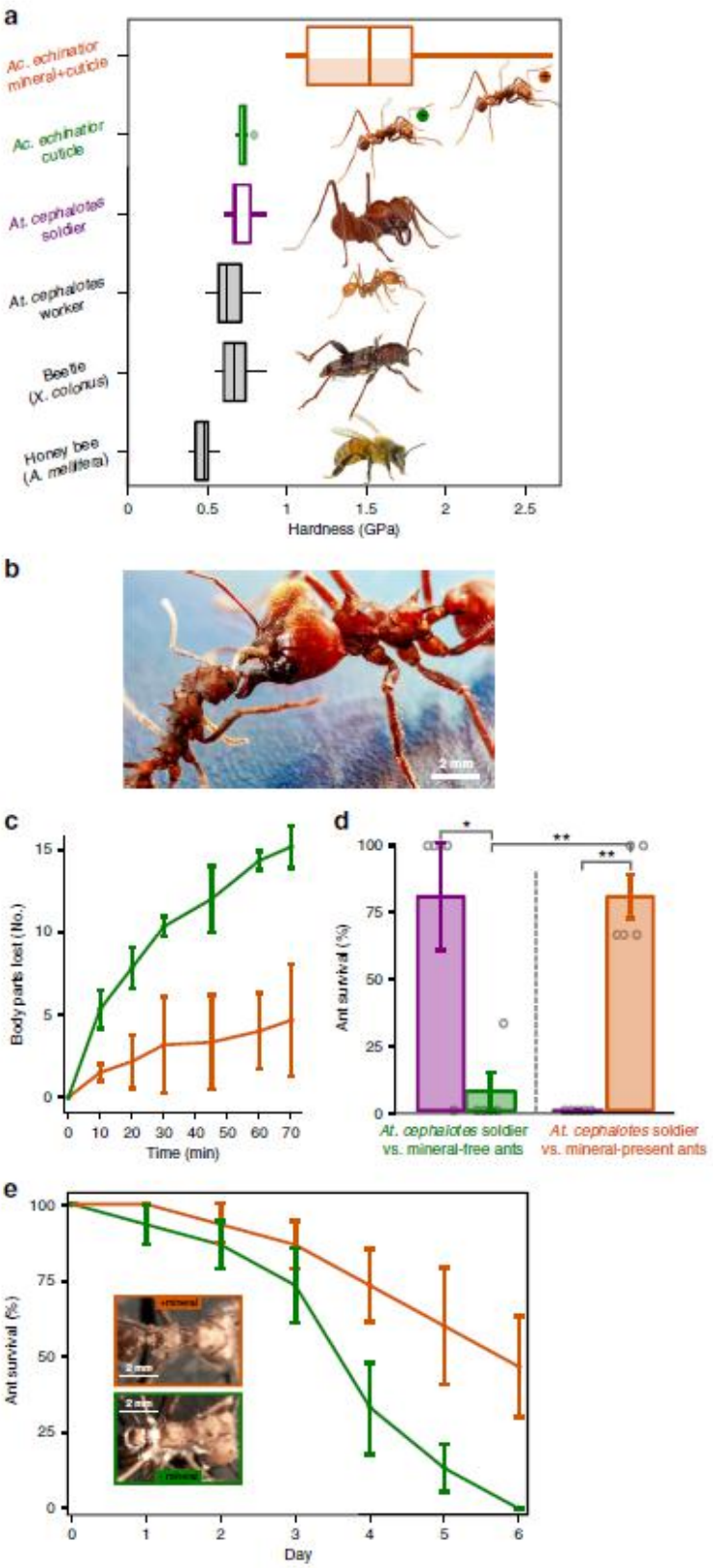

Figure 3. Mechanical protection afforded by the epicuticular mineral layer. a Quantitative nano-mechanical properties of insect cuticles, including honeybee (Apis mellifera), beetle (Xylotrechus colonus), leaf-cutting ants [Atta cephalotes worker, Atta cephalotes soldier (purple), and Acromyrmex

echinatior worker without biomineral (green, with green minus circle beside the ant image)] and Ac. echinatior ant worker with biomineral epicuticular layer (orange, with orange plus circle beside the ant image), measured by an in situ nanoindenters with a cube-corner probe (n = 12, 15, 13, 15, 12, and 13 for insect measured above, respectively; center, median; box, upper and lower quantiles; whisker, 1.5 × interquartile range; points, outlier). Atta ants images, Xylotrechus beetle image, and Apis bee image provided with permission from the copyright holder, Alexander L. Wild, Jon Rapp, and Don Farrall, respectively. b–d Aggressive interaction between three Ac. echinatior workers (with/without biomineral, respectively) and Atta cephalotes soldier (Photo C.M.C.). b Ac. echinatior worker (left) aggressively interacts with Atta cephalotes soldier (right). c In aggressive encounters with Atta cephalotes soldiers, Ac. echinatior workers with biomineral armor (orange) lose substantially fewer body parts (i.e., legs, antennae, abdomen, and head) compared to Ac. echinatior worker without biomineral (green). d Survivorship of Ac. echinatior workers without (green) and with (orange) biomineral armor in aggressive encounters with Atta cephalotes soldiers (purple). Asterisks indicate significant differences via a two-sample t-test (*P < 0.05, **P < 0.001; P-value = 0.0184, 0.0001, and 0.0006 from left to right, respectively; n = 5 per treatment and the corresponding standard error are shown.). e Survivorship curves of Ac. echinatior worker with (orange) and without (green) an epicuticular biomineral layer exposed to the entomopathogenic fungus Metarhizium. The inset images show more substantial fungal growth and emergence from biomineral-free workers (Photo H.L.). c, e n = 3 per treatment, and the corresponding standard error.

3. 三叠纪末期大西洋中部岩浆省中的深部 CO_2

翻译人：冯婉仪 fengwy@sustech.edu.cn

Capriolo M, Marzoli A, Aradi L E, et al. ***Deep CO_2 in the end-Triassic Central Atlantic Magmatic Province*** *[J]. Nature Communications, 2020, 11: 1670.*

https://doi.org/10.1038/s41467-020-15325-6

摘要：大火成岩省的喷发与显生宙的许多大灭绝事件同时发生，表明了火山去气作用触发全球气候变化的因果关系。为了充分认识这一关系，有必要限定去气岩浆挥发份的数量和类型，并且确定其来源的深度和喷发时间。通过对熔融包裹体内保存的气体出溶气泡的研究，我们提供了三叠纪末期大西洋中部岩浆省（CAMP）玄武岩中富含 CO_2 的直接证据。我们的结果表明 CO_2 的含量以及至少有一部分去气碳来自地幔和/或中-下地壳。深部碳的存在是控制 CAMP 岩浆侵位模式的关键因素，它有利于形成快速喷发的脉冲（每次都是几个世纪）。我们的估算表明，每一次 CAMP 岩浆脉冲注入三叠纪末期大气中的 CO_2 量与 21 世纪预测的人为排放量相当。如此大量的火山 CO_2 可能导致了三叠纪末期的全球变暖和海洋酸化。

ABSTRACT: Large Igneous Province eruptions coincide with many major Phanerozoic mass extinctions, suggesting a cause-effect relationship where volcanic degassing triggers global climatic changes. In order to fully understand this relationship, it is necessary to constrain the quantity and type of degassed magmatic volatiles, and to determine the depth of their source and the timing of eruption. Here we present direct evidence of abundant CO_2 in basaltic rocks from the end-Triassic Central Atlantic Magmatic Province (CAMP), through investigation of gas exsolution bubbles preserved by melt inclusions. Our results indicate abundance of CO_2 and a mantle and/or lower-middle crustal origin for at least part of the degassed carbon. The presence of deep carbon is a key control on the emplacement mode of CAMP magmas, favouring rapid eruption pulses (a few centuries each). Our estimates suggest that the amount of CO_2 that each CAMP magmatic pulse injected into the end-Triassic atmosphere is comparable to the amount of anthropogenic emissions projected for the 21st century. Such large volumes of volcanic CO_2 likely

contributed to end-Triassic global warming and ocean acidification.

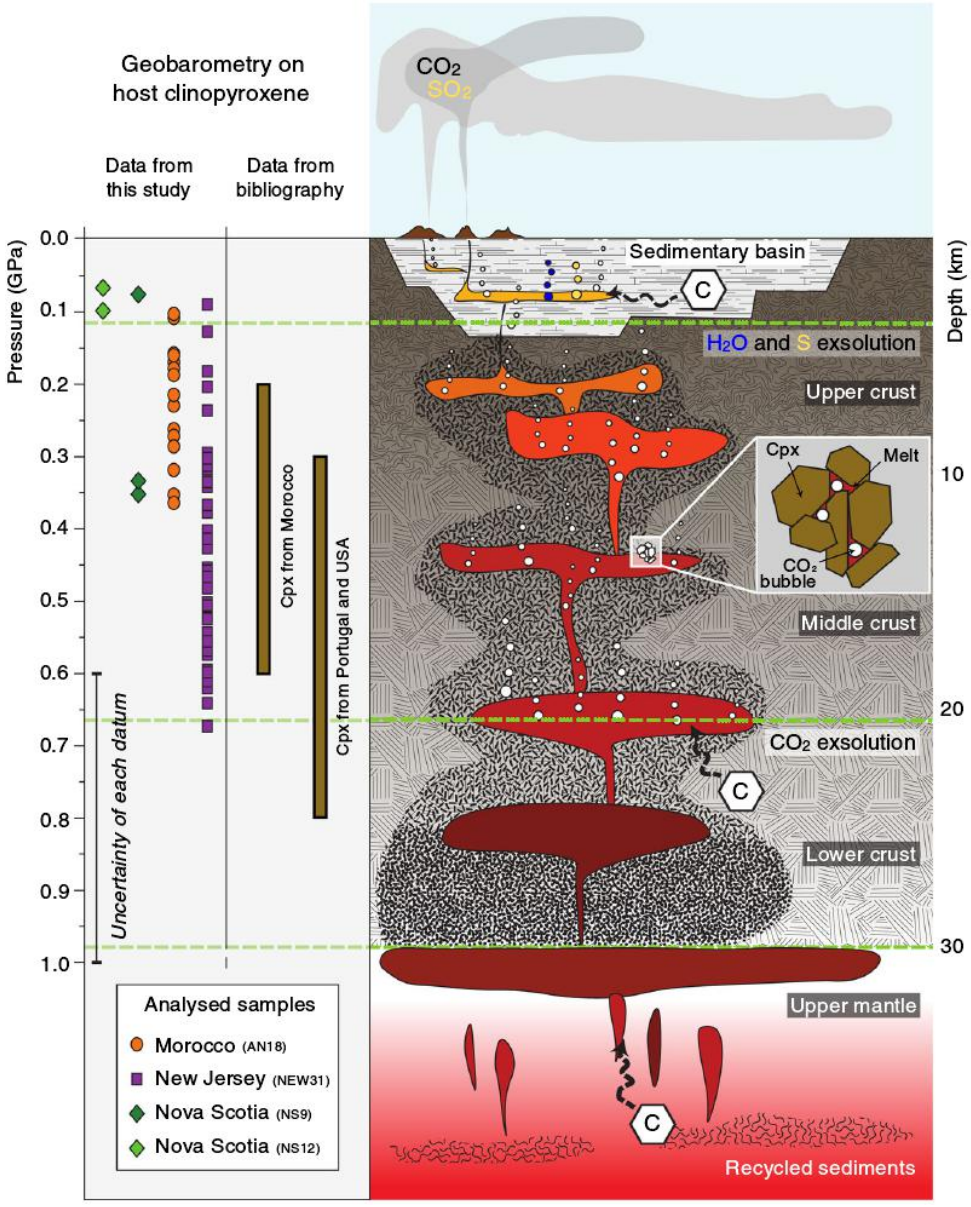

Figure 1. Sketch of the transcrustal plumbing system of CAMP basaltic magmas from the mantle to the surface. The evolution of basaltic magmas occurs at variable depth by crystallization of minerals, which then form aggregates in crystalline mushes[13,14] and entrain bubble-bearing melt, forming MIs. Different volatile species exsolve at variable depth16. In particular, CO_2-rich fluids (white bubbles) start exsolving at great depth, whilst H_2O-rich fluids (blue bubbles) and S-rich fluids (yellow bubbles) start exsolving at shallow depth. The black dashed arrows indicate the potential sources for the carbon in CAMP magma: the mantle, the deep crust and the Palaeozoic or Triassic sedimentary basins in which CAMP sills intruded. The carbon within the here studied MIs derives from the deep sources as

demonstrated with clinopyroxene geobarometry data. Clinopyroxene crystallization pressures of this study have been calculated using ref. [37] (Supplementary Note 2). Clinopyroxene crystallization pressures of bibliography are from ref. [23] for Morocco, ref. [39] for Portugal, and ref. 40 for USA. The error (± 0.2 GPa) takes into account the uncertainties from both the geobarometry model (± 0.1 GPa)[37] and the electron microprobe analyses (± 0.1 GPa, deriving from the ± 10% accuracy on measured Na concentration).

4. 83.0-42.5 Ma 中印度洋详细的结构和板块重建

翻译人：李园洁 liyj3@sustech.edu.cn

Yatheesh V, Dyment J, Bhattacharya G C, et al. ***Detailed structure and plate reconstructions of the Central Indian Ocean between 83.0 and 42.5 Ma (Chrons 34 and 20)*** *[J]. Journal of Geophysical Research: Solid Earth, 2019, 124: 4305-4322.*

https://doi.org/0.1029/2018JB016812

摘要：中印度洋也就就是中印度洋盆，Crozet 洋盆和马达加斯加洋盆，形成于印度板块（现在的 Capricorn），南极洲板块和非洲板块（现在的 Somalia）的裂解和之后的漂移。本文作者收集了穿过这些洋盆的海平面观测的磁异常剖面，利用目标解析信号方法重新识别出 C34ny（83.0 Ma）到 C20ny（42.536 Ma）的磁异常等时线。基于~ 1400 个磁异常特征点得到 29 个时期的高分辨率等时线。通过共轭的特征点，可得到 Capricorn-Antarctica 和 Capricorn-Somalia 的两个板块的有限旋转参数。与 Capricorn，Antarctica，Somalia 板块之间板块边界的重建进行比较。整体上，三个板块的重建相对 Capricorn-Antarctica 和 Capricorn-Somalia 的两个板块的重建稍微过度旋转。而 Somalia-Antarctica 的两个板块的重建相对三个板块的重建稍微旋转不足。作者认为两个板块和三个板块的重建之间的差异可能来自 Capricorn-India 扩散边界最近的海底变形或不同扩张速率的磁异常等时线的本质和几何形态的差异（比如三个扩张中心的磁结构）。三个板块的重建可更好约束三联点的闭合，但三个板块边界都可能存在误差。如果有质量足够高的数据，两个板块的重建可得到更可靠的板块运动。

ABSTRACT： The Central Indian Ocean, namely the Central Indian, Crozet, and Madagascar basins, formed by rifting and subsequent drifting of India (now Capricorn), Antarctica, and Africa (now Somalia). We gathered a comprehensive set of sea surface magnetic anomaly profiles over these basins and revisited location and identification of magnetic isochrons between C34ny (83.0 Ma) and C20ny (42.536 Ma) using the objective analytic signal technique. We present

high-resolution magnetic isochrons for 29 periods based on ~1,400 magnetic anomaly picks. From the conjugate sets of picks, we derive two-plate finite rotation parameters for both the Capricorn-Antarctica and Capricorn-Somalia motions. These finite rotations are compared to three-plate reconstructions of the plate boundaries between the Capricorn, Antarctica, and Somalia plates, constrained by the closure of the Indian Ocean Triple junction. In general, the three-plate reconstructions slightly overrotate the reconstructed isochrons with respect to the Capricorn-Antarctica and Capricorn-Somalia two-plate reconstructions. Conversely, the two-plate reconstructions for Somalia-Antarctica slightly underrotate the isochrons compared to the Capricorn-Antarctica-Somalia three-plate reconstructions. We suspect that the discrepancies between the two-plate and three-plate methods result from the recent seafloor deformation in the Capricorn-India diffuse plate boundary and/or from the contrasted nature and geometry of magnetic isochrons at different spreading rates (i.e., magnetic structure of the three spreading centers). Three-plate reconstructions better constrain the closure of the triple junction but spread any misfit among all three plate boundaries. When enough quality data are available, two-plate reconstructions may lead to more realistic plate motion estimates from which additional geological problems can be identified and solved.

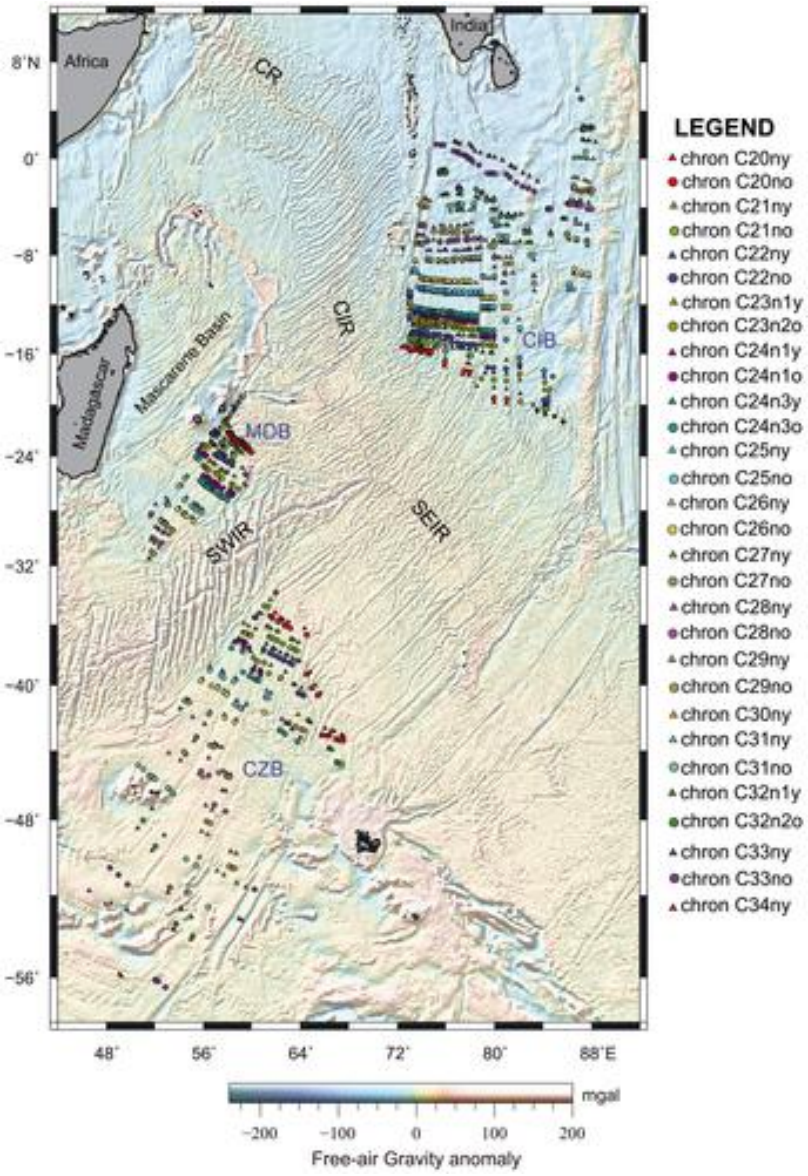

Figure 1. Updated magnetic anomaly picks superposed on satellite-derived free-air gravity anomaly map in the Central Indian Ocean. Age of the lineations are indicated by colors as in the legend.

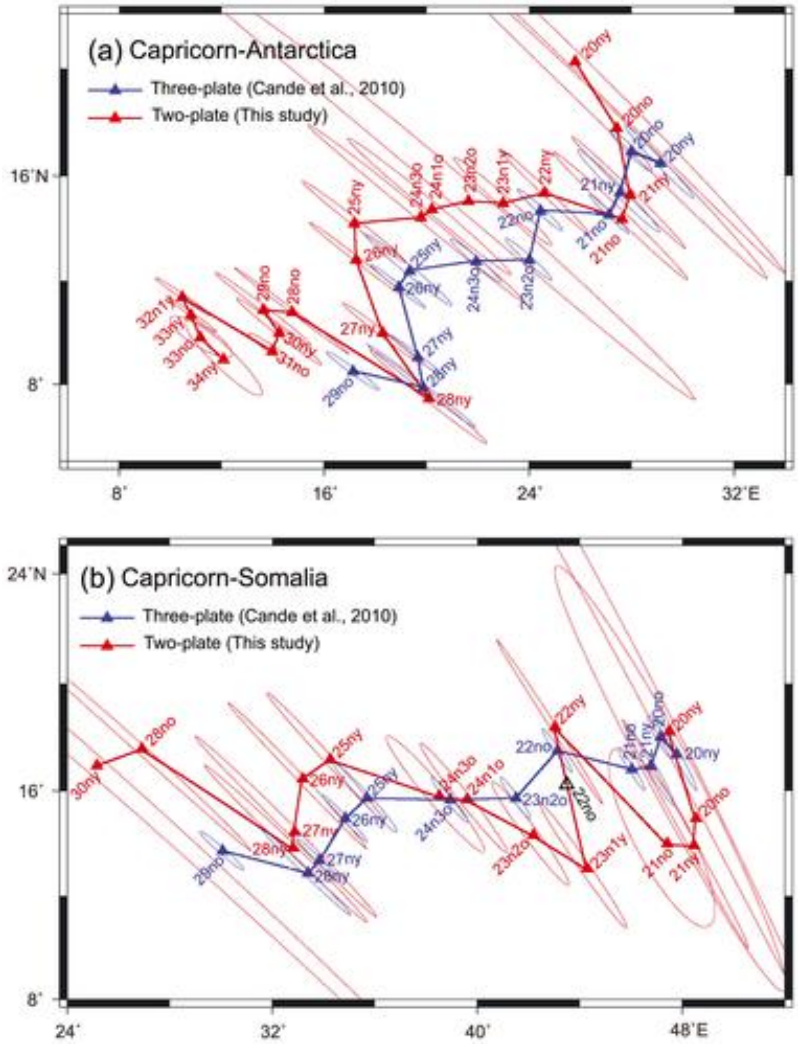

Figure 2. Location and ellipse error of finite rotation poles for Capricorn-Antarctica (a) and Capricorn-Somalia (b) for the two-plate (red, Table 3) and three-plate (blue, Cande et al., 2010) reconstructions. On (b), the open black triangle marks the finite rotation pole for Chron C22no (16.252 °N, 43.554 °E, −27.040 °), which is not listed in Table 3 but reinforces our confidence in the observed fluctuation between Chrons C23 and C21.

5. 基于 WACCM-X 模型对过去 1950-2015 年高层大气气候变化的分析

翻译人：柳加波 Liujb@sustech.edu.cn

*Cnossen I. **Analysis and attribution of climate change in the upper atmosphere from 1950 to 2015 simulated by WACCM‐X [J]. Journal of Geophysical Research: Space Physics, 2020: e2020JA028623.***

https://doi.org/10.1029/2020JA028623

摘要：监测高层大气中热层和电离层的气候变化并了解其原因具有重要的现实意义。为支持这些工作并促进观测结果与模型结果之间的比较，我们使用 Whole Atmosphere Community Climate Model eXtension (WACCM-X)模型对 1950 至 2015 年间进行了长期瞬态模拟。该模型使用了所有已知的高层大气气候变化的驱动因素，包括了太阳和地磁活动、主要磁场变化以及痕量气体排放（包括 CO_2）的实际变化。标准多线性回归方法对整个 1950-2015 年的分析表明，很难充分消除太阳周期效应以获得可靠的趋势。除了 F10.7a、K_P 和趋势本身的代数项外，当回归模型中包含$(F10.7a)_2$时，模型结果也会得到改善。与以前的研究和空间变化趋势估算分析对比证实，CO_2 浓度的增加是热层温度和密度变化趋势的主要驱动因素，但在高（磁）纬度，主要磁场变化的影响也起着同样作用，特别是在北半球。h_mF_2，N_mF_2 和总电子含量趋势的空间特征表明，CO_2 和地磁场效应是叠加的，后者在~ 50–20 °N，~ 60 °W 至 20 °E 的区域内占主导地位。其他模型实验研究了低层大气（< 50 km）对高层大气（> 100 km）的气候变化的间接动力学影响，表明这些影响很小且微不足道。但是，当前模型的局限性可能意味着这些影响被低估了。

ABSTRACT: Monitoring climatic changes in the thermosphere and ionosphere and understanding their causes is important for practical purposes. To support this effort and facilitate comparisons between observations and model results, a long transient simulation with the Whole Atmosphere Community Climate Model eXtension (WACCM-X) from 1950 to 2015 was conducted. This simulation used realistic variations in solar and geomagnetic activity, main magnetic field changes, and trace gas emissions, including CO_2, thereby including all known

drivers of upper atmosphere climate change. Analysis of the full 1950–2015 interval with a standard multilinear regression approach demonstrated difficulties in removing solar cycle effects sufficiently to obtain reliable trends. Results improved when an $(F10.7a)^2$ was included in the regression model, in addition to terms for $F10.7a$, K_P, and the trend itself. Comparisons with previous studies and analysis of spatial variations in trend estimates confirmed that the increase in CO_2 concentration is the main driver of trends in thermosphere temperature and density, but at high (magnetic) latitudes effects of main magnetic field changes play a role as well, especially in the Northern Hemisphere. Spatial patterns of trends in h_mF_2, N_mF_2, and total electron content indicate a superposition of CO_2 and geomagnetic field effects, with the latter dominating trends in the region of ~ 50–20 °N, ~ 60 °W to 20 °E. Additional model experiments to investigate the indirect dynamical effects of climate change in the lower atmosphere (< 50 km) on the upper atmosphere (> 100 km) suggested that these effects are small and insignificant. However, current model limitations could mean that these effects are underestimated.

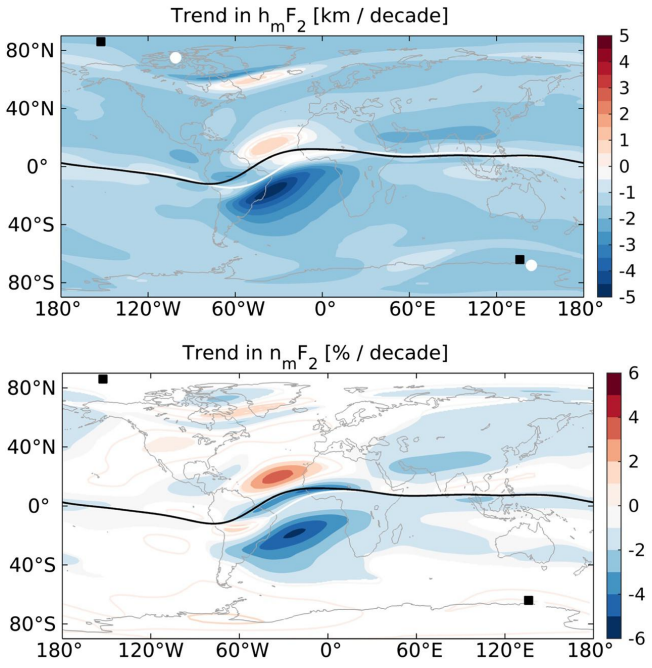

Figure 1. Trends in h_mF_2 (km/decade, top) and N_mF_2 (%/decade, bottom). Filled contours indicate that trends are statistically significant at the 95% confidence level, while line contours are used for nonsignificant trends. The location of the magnetic equator and magnetic poles in 1950 (2015) are marked with a white (black) line and white circles (black squares), respectively.

6. 晚始新世长江第一湾的形成导致了长江的诞生

翻译人：刘伟 inewway@163.com

Zheng H, Clift P D, He M, et al. ***Formation of the First Bend in the late Eocene gave birth to the modern Yangtze River, China*** *[J]. Geology, 2020.*

https://doi.org/10.1130/G48149.1

摘要：长江第一湾，也就是河流停止向南流和开始向东北流的地点，一直是亚洲最具争议的地貌特征点。因为它的形成对理解长江的历史和有关青藏高原东南缘的构造隆升特别关键。紧靠长江第一湾西南方向的剑川盆地中-上始新世沉积岩显示了一个大水系（可能是古金沙江(长江上游)水系）曾向南流经该地区。基于碎屑锆石 U-Pb 定年，对该区沉积物源进行分析，证实了曾南流的古长江起源于青藏高原，并汇入南海。伴随着高原隆起，开始于始新世或之后的剑川盆地构造反转，导致江水向东北改道，且流向受限于与走滑断裂有关的构造线。这个改道就导致了现代长江的诞生。

ABSTRACT: The First Bend on the Yangtze River (China), the point where the river ceases flowing toward the south and heads toward the northeast, has been one of the most strongly debated geomorphic features in Asia because it holds the key to understanding the history of the Yangtze River and is linked to the tectonically driven surface uplift of the southeastern Tibetan Plateau. Mid- to upper Eocene sedimentary rocks preserved in the Jianchuan Basin located immediately southwest of the First Bend demonstrate that a large river system, presumably the paleo–Jinshajiang River (the upper Yangtze), used to flow south through that region. Provenance analysis of sediments over the wider region, based mostly on U-Pb dating of detrital zircon grains, confirms that the once south-flowing paleo–Yangtze River originated in the Tibetan Plateau and flowed into the South China Sea. Inversion of the Jianchuan Basin, starting in or after the latest Eocene and associated with wider plateau surface uplift at that time, caused the river to be diverted toward the northeast where it was confined along tectonic lineaments associated with strike-slip faulting, giving birth to the First Bend, a major step in the formation of the modern

Yangtze River.

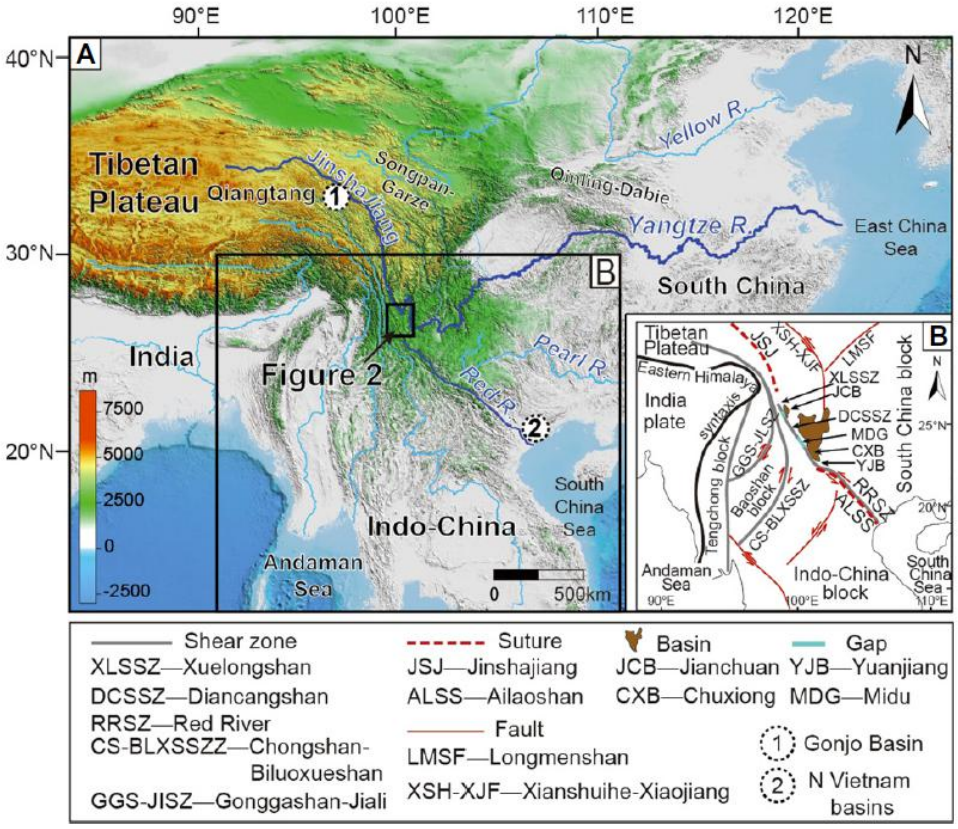

Figure 1. The First Bend on the Yangtze River (China), the point where the river ceases flowing toward the south and heads toward the northeast, has been one of the most strongly debated geomorphic features in Asia because it holds the key to understanding the history of the Yangtze River and is linked to the tectonically driven surface uplift of the southeastern Tibetan Plateau. Mid- to upper Eocene sedimentary rocks preserved in the Jianchuan Basin located immediately southwest of the First Bend demonstrate that a large river system, presumably the paleo–Jinshajiang River (the upper Yangtze), used to flow south through that region. Provenance analysis of sediments over the wider region, based mostly on U-Pb dating of detrital zircon grains, confirms that the once south-flowing paleo–Yangtze River originated in the Tibetan Plateau and flowed into the South China Sea. Inversion of the Jianchuan Basin, starting in or after the latest Eocene and associated with wider plateau surface uplift at that time, caused the river to be diverted toward the northeast where it was confined along tectonic lineaments associated with strike-slip faulting, giving birth to the First Bend, a major step in the formation of the modern Yangtze River.

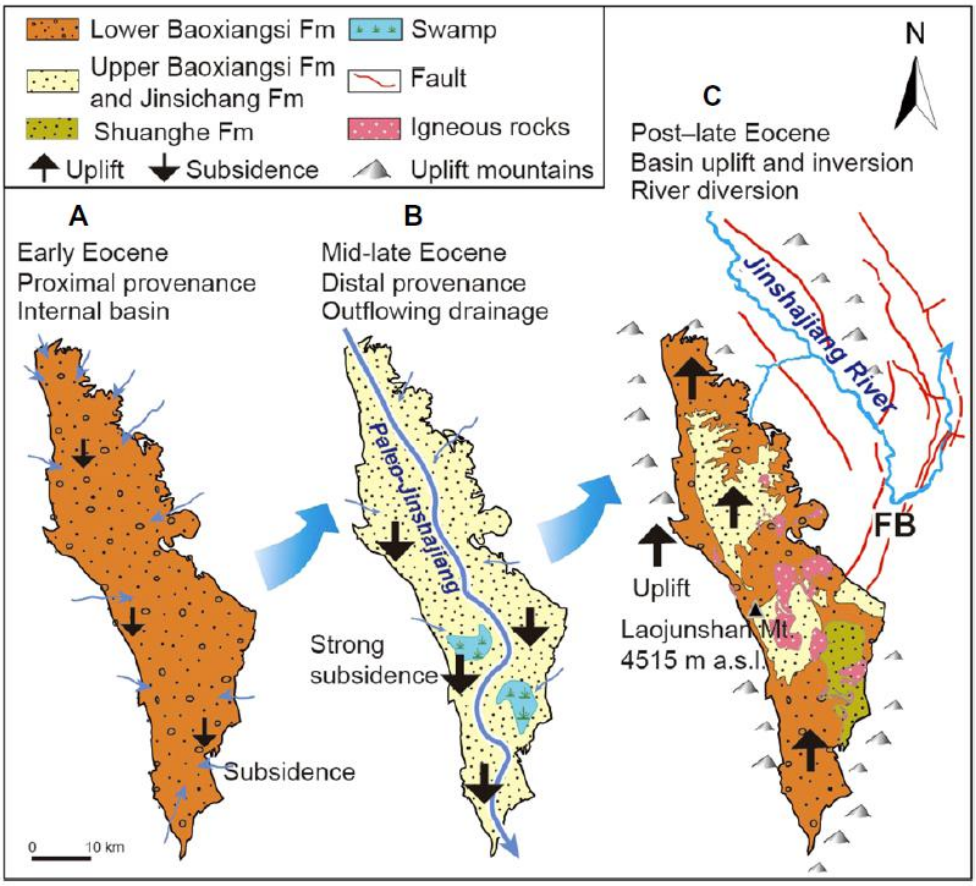

Figure 2. Sketch maps illustrating formation processes of First Bend of Yangtze River. (A) Jianchuan Basin as internal basin during early Eocene. (B) External basin with outflowing paleo–Jinshajiang River during mid- to late Eocene. (C) Inversion of basin during late Eocene diverted paleo-Jinshajiang to east to form First Bend. Faults are from Yunnan Bureau of Geology and Mineral Resources (1990). a.s.l.—above sea level; FB—First Bend.

7. 通过一百多个钻孔数据发现：一种根据磁测图与测井磁化率数据确定土壤 Koenigsberger 比值的新方法

翻译人：曹伟 11930854@QQ.com

Pickartz, N, Rabbel, W, Rassmann, K, et al. ***What over 100 drillings tell us: a new method for determining the Koenigsberger ratio of soils from magnetic mapping and susceptibility logging*** *[J]. Archaeological Prospection. 2020, 27: 393-414.*

https://doi.org/10.1002/arp.1782

摘要：为了进一步发展剩磁作为考古磁测解释的附加参数，我们对新石器时代长坑充填物的剩余磁化强度和感应磁化强度的相对分数进行了研究。通过将磁测数据与井下磁化率测量、数值模拟和反演计算相结合，我们确定了关键目标的 Koenigsberger 比率-感应磁化强度和剩余磁化强度之间的比值。磁化率数据是通过磁测识别目标断面上的钻孔获得的。这项示范性研究的目标是 Linearbandkeramik 遗址（Vráble Farské）的房屋附属坑。为此，我们进行了点距为 25 cm 的螺旋钻钻井，并用井下磁化率仪测量了磁化率。利用得到的二维磁化率分布计算了单独磁化情况下的合成磁异常。计算结果与观测数据显示出较大差异，因此只能通过剩余磁化强度来解释。为了确定 Koenigsberger 比值，我们开发了一种新的解释方法，使用部分测量的磁化率分布作为基函数。该数值问题的自由参数由非线性反演确定。我们将新方法应用于六个典型剖面，发现 Koenigsberger 比值在 1.6 到 10.5 之间，大多数值小于 4。这些值适用于磁化率值大于 27-160×10-5 SI 的土壤体积。土壤样品的实验室测量结果被用来分析造成观测磁化强度的可能原因。分析表明，坑内磁化率和剩余磁化强度的增加是由于趋磁细菌数量的增加和磁化物质的沉积所致，其次是铁磁性化合物在浸水环境中的凹坑排列和粘滞剩磁的积累。

ABSTRACT: We investigate the relative fractions of remanent and induced magnetization of the fillings of neolithic long pits in order to develop remanent magnetization as an additional parameter for the archaeological interpretation of magnetic maps. We determine the Koenigsberger ratio-the ratio between induced and remanent magnetization intensities - for key targets by combining magnetic mapping with downhole measurements of susceptibility, numerical

modelling, and inversion computations. The susceptibility data were acquired in drill holes along profiles crossing the targets identified by magnetic mapping. The targets of this exemplary study are house-accompanying pits at the Linearbandkeramik site Vráble ‘Farské’. For this purpose, we conducted auger drillings with a point distance of 25 cm and measured the susceptibility with a downhole susceptometer. The resulting two-dimensional susceptibility distributions were used to calculate synthetic magnetic anomalies corresponding to the case of solely induced magnetization. The comparison to the observed magnetic data showed a considerable discrepancy that can only be explained with remanent magnetization. To determine the Koenigsberger ratio we developed a new interpretation approach, using parts of the measured susceptibility distribution as a basis function. The free parameters of this numerical problem are determined by non‐linear inversion. We applied the novel approach to six exemplary profiles and found Koenigsberger ratios between 1.6 and 10.5 with the majority of the values being smaller than 4. These values apply to soil volumes with susceptibility values larger than 27-160×10-5 SI. Laboratory measurements on soil samples were used to examine the possible causes of the observed magnetization. The analyses suggest that the increase in susceptibility and remanent magnetization in the pits is caused by an increase of the population of magnetotactic bacteria and deposition of magnetized material, followed by the alignment of the ferrimagnetic iron compounds in the waterlogged environment of the pits and accumulation of viscous remanent magnetization.

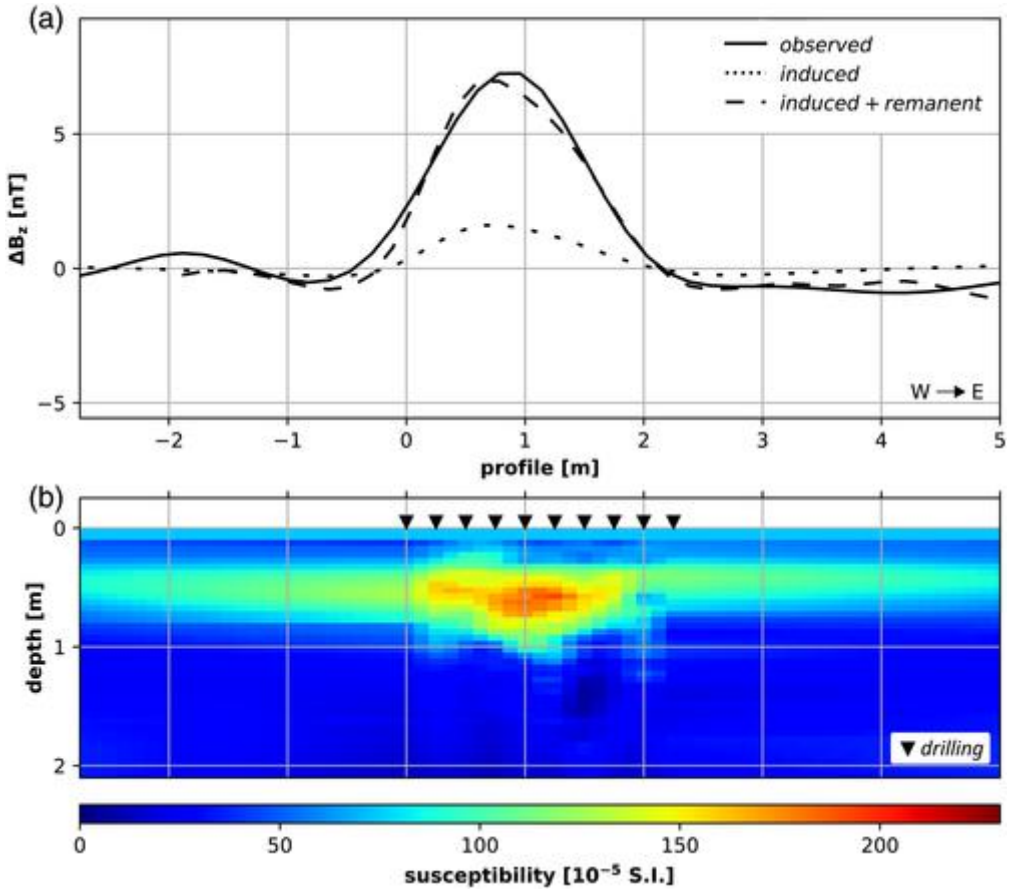

Figure 1. (a) Measured magnetic profile (vertical component gradiometer data) and calculated magnetic anomaly assuming induced (dotted line) and induced plus remanent (dashed line) soil magnetization. The dashed line shows the optimum fit obtained for a Koenigsberger ratio Q of 2.4 for subsurface points with a susceptibility $\kappa \geq 90\times10^{-5}$ SI, and Q = 0 elsewhere. The underlying two-dimensional susceptibility distribution is shown in (b). Downhole measurements of magnetic susceptibility were performed at the drilling locations indicated by black triangles. Outside this area the values were extrapolated and tapered to the average κ-depth function of the surrounding soil.

8. 全球气候、风尘以及铁元素生物地球化学之间的联系

翻译人：王敦繁 dunfan-W@foxmail.com

Jickells T D. ***Global Iron Connections Between Desert Dust, Ocean Biogeochemistry, and Climate*** *[J]. Science, 2005, 308: 67-71.*

https://doi.org/10.1126/science.1105959

摘要：地球的环境条件，包括气候，是由物理、化学、生物和人类相互作用决定的，这些相互作用转化和运输物质和能源。这就是“地球系统”：一个高度复杂的实体，具有多个非线性响应和阈值，不同的部件之间存在联系。这个系统的一个重要部分是铁循环，在这个循环中，含铁的土壤尘埃从陆地通过大气转移到海洋，影响海洋生物地球化学，从而对气候和尘埃产生反馈作用。这里我们回顾了这个周期的关键组成部分，阐明了未来研究的关键和不确定性。

ABSTRACT: The environmental conditions of Earth, including the climate, are determined by physical, chemical, biological, and human interactions that transform and transport materials and energy. This is the ‘‘Earth system’’: a highly complex entity characterized by multiple nonlinear responses and thresholds, with linkages between disparate components. One important part of this system is the iron cycle, in which iron- containing soil dust is transported from land through the atmosphere to the oceans, affecting ocean biogeochemistry and hence having feedback effects on climate and dust production. Here we review the key components of this cycle, identifying critical uncertainties and priorities for future research.

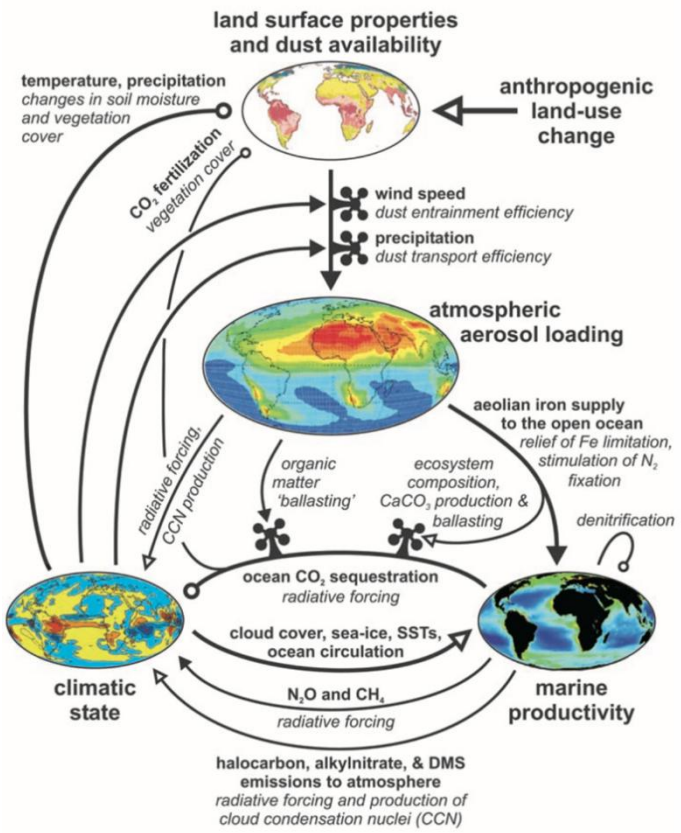

Figure 1: Schematic view of global iron and dust connections. Highlighted are the four critical components (clockwise from top): the state of the land surface and dust availability, atmospheric aerosol loading, marine productivity, and some measure of climatic state (such as mean global surface temperature). The sign of the connections linking these varies; where the correlation is positive (for example, increased atmospheric aerosol loading Y increased marine productivity), the line is terminated with a solid arrowhead. Where the correlation is negative (for example, increased marine productivity Y lower CO2 and a colder climate), the termination is an open circle. Connections with an uncertain sign are terminated with an open arrowhead. The mechanism by which the link acts (for example, the impact of a change in atmospheric CO2 is via the radiative forcing of climate) is displayed in italics. Finally, the ‘‘water tap’’ symbols represent a secondary mechanism modulating the effect of a primary mechanism; for instance, a change in global precipitation strength and distribution will alter the efficiency with which entrained dust is transported to the open ocean. If a path of successive connections can be traced from any given component back to itself, a closed or feedback loop is formed. An even number (including zero) of negatively correlated connections counted around the loop gives a positive feedback, which will act to amplify a perturbation and tend to destabilize the system.

Conversely, an odd number of negative correlations gives a negative feedback, dampening any perturbation and thus stabilizing the system. For instance, atmospheric aerosol loading Y marine productivity Y climatic state Y dust availability Y atmospheric aerosol loading contains two negative and two positive correlations and thus is positive overall. In contrast, marine productivity looping back onto itself contains a single negative correlation and thus represents a negative feedback.

Table 2. Effects of dust/iron (Fe) on ocean biogeochemistry. (In addition, there are dust effects on the climate system via albedo and the hydrological cycle; see text.)

Interaction	Mechanism	Area*	Reference
Primary productivity	Reduction in Fe limitation allows more efficient use of macronutrients and hence CO_2 uptake.	HNLC and other Fe-limited areas	(*36*, *42*)
N_2 fixation	Reduction in Fe limitation on nitrogen fixation increases primary production and hence CO_2 uptake.	Subtropical gyres	(*1*, *43*)
Changes in species composition	Species-selective relief of iron stress.	Global	(*42*)
Ballast effect	Increases sinking rate of organic matter, reducing organic matter regeneration within seasonal mixed layer; promotes CO_2 uptake.	Probably only significant in areas of high dust deposition	(*52*)
DMS	Increased productivity leads to increased DMS emissions and increased aerosol formation.	HNLC and other Fe-limited areas	(*54*)
N_2O and NO_3^-	Increased fluxes of organic matter to deep waters lower oxygen concentrations and promote denitrification, release N_2O, and lower oceanic nitrate inventory.	Upwelling systems	(*53*)
N_2O and CH_4	Increased productivity leads to changes in euphotic zone methane and N_2O concentrations.	HNLC and other Fe-limited areas	(*54*, *57*)
H_2S	Increased fluxes of organic matter to deep waters lower oxygen concentrations and promote sulfate reduction; sulphide production lowers iron inventory.	Upwelling systems	
Halocarbons and alkyl nitrates	Biogenic gases linked to primary productivity. These are greenhouse gases, linked to aerosol formation and to the ozone cycle.	As for DMS	(*54*)
Isoprene and CO	Biogenic trace gases linked to primary productivity. These gases influence atmospheric oxidizing capacity.	As for DMS	(*54*, *57*)

*Most impacts have effects throughout the oceans, but where appropriate, we identify here areas that are most sensitive to changes in dust/iron flux.

9. 太平洋十年际涛动推动了格陵兰地区最后一次冰盛期地表温度变化的增强过程

翻译人：王浩森 11930841@mail.sustech.edu.cn

*Song Z, Latif M, Park W, et al.. **Interdecadal Pacific Oscillation Drives Enhanced Greenland Surface Temperature Variability During the Last Glacial Maximum** [J]. Geophysical Research Letters, 2020, 47: e2020GL088922.*

https://doi.org/10.1029/2020GL088922

摘要：稳定的氧同位素记录代表了地表气温（SAT），来自格陵兰中部的记录表明从上一个冰期（上一次冰盛期，LGM；大约 21,000 年之前）到近代，十年间的年代际变率成比例地减少。根据气候模型可模拟出多年的格陵兰 SAT 的变化。 LGM 期间增强的变化很大程度上是由年代际太平洋涛动（IPO）远程驱动的，这是一种太平洋海面温度（SST）的十年际振荡。在冰期，大气层与 IPO 的遥相关性不断增强，促使格陵兰岛的地表风增强，并通过大气热传输使 SAT 发生变化。

ABSTRACT: Stable oxygen isotope records, a proxy for the local surface air temperature (SAT), from central Greenland indicate disproportionally large reductions in the multidecadal variability from the Last Ice Age (Last Glacial Maximum, LGM; about 21,000 years before present) to modern times. A climate model simulates the changes in multidecadal Greenland SAT variability as inferred from the proxy data. The enhanced variability during the LGM is largely remotely driven by the Interdecadal Pacific Oscillation (IPO), a multidecadal oscillation of sea surface temperature (SST) in the Pacific Ocean. Atmospheric teleconnections from the IPO strongly intensify under glacial conditions, driving enhanced surface wind variability over Greenland and through atmospheric heat transport the SAT variability.

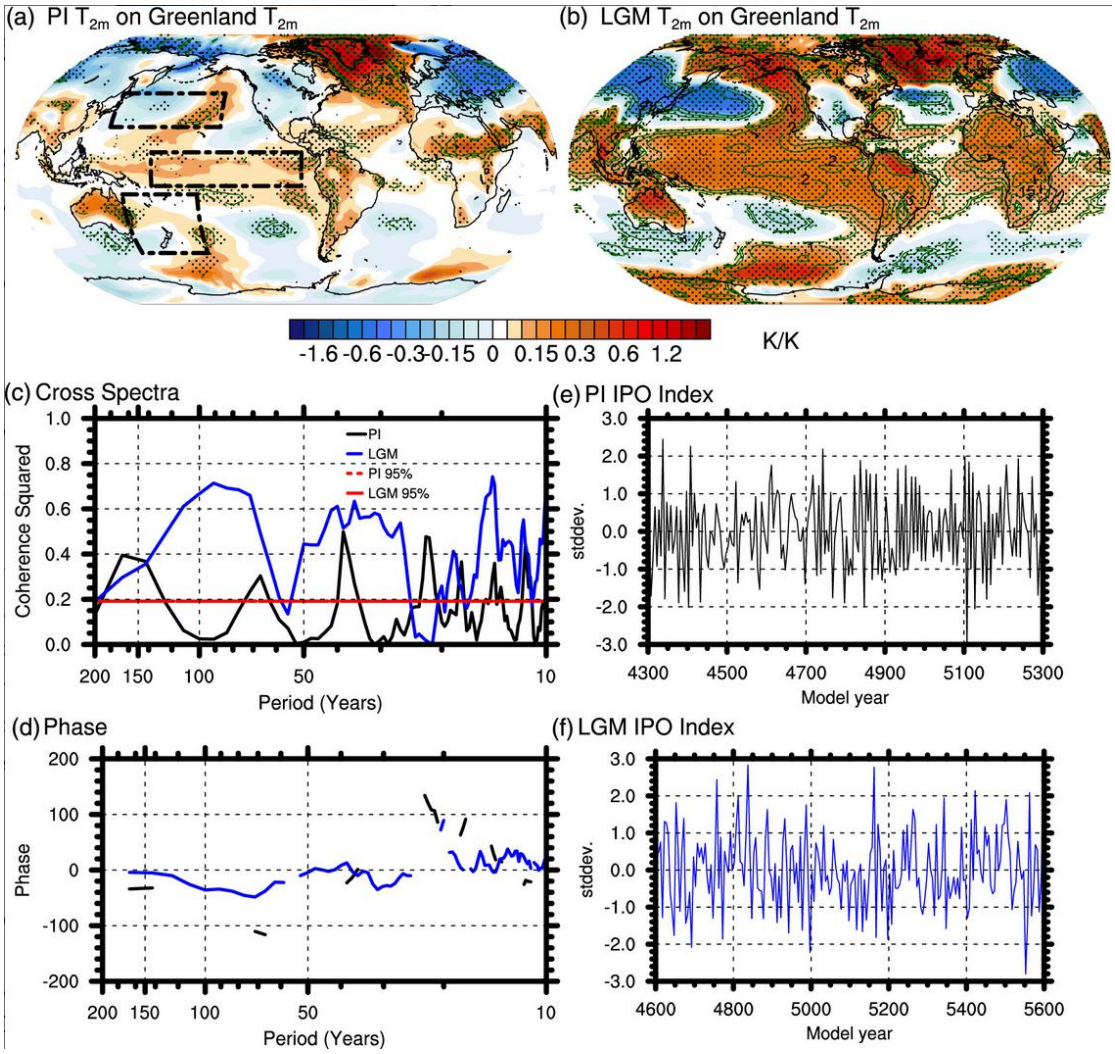

Figure 1. Regressions (K/K) of 5-year mean SAT anomalies on the 5-year mean SAT averaged over Greenland for the (a) PI and (b) LGM simulations. Stippling indicates significance at the 95% confidence interval using *p* value test. (c, d) Results from cross-spectral analysis between the tripole IPO index and Greenland SAT. (c) Squared coherence spectrum of the IPO index and Greenland SAT in the PI and LGM experiments. The red dashed and solid lines indicate the 95% confidence limit for the squared coherence. (d) Phase spectrum between the IPO index and Greenland SAT. Positive phase refers to the IPO index leading the variations in Greenland SAT. Note that phase only is shown at frequencies with statistically significant squared coherence. 5-year mean IPO index in the (e) PI (black) and (f) LGM (blue).

10. D-O 旋回的一种冰-气候震荡模式

翻译人：郑威　11930589@mail.sustech.edu.cn

Menviel L C, Skinner L C, Tarasov L, et al. ***An ice–climate oscillatory framework for Dansgaard–Oeschger cycles*** *[J]. Nature Reviews Earth & Environment, 2020: 1-17.*

https://doi.org/10.1038/s43017-020-00106-y

摘要：间冰期以格陵兰岛和北大西洋温度大幅变化为特征，被称为Dansgaard–Oeschger（D-O）变化，其中一些变化持续几十年。D-O变化包括大西洋经向翻转流（AMOC）强度的改变，各半球反向和异时性的温度变化，热带辐合带（ITCZ）的平均位置和大气二氧化碳的变化。古记录和数值研究表明，AMOC与北欧海冰有紧密的耦合关系，是D-O变化的核心，然而，还未有一个完善的理论。在这篇综述中，我们综合了气候表达和过程来解释D-O旋回，浮现出一个通过大气、冰冻圈和地球生物化学系统反馈而产生的AMOC-海冰的震荡结构。古气候观测表明，AMOC可能比现在的气候模型对扰动更为敏感。因此，需要严格限制AMOC的稳定性来预测下个世纪人为碳排放引起的AMOC的变化。未来有望通过额外的观测限制和气候-冰盖耦合模型数值模拟来取得进展。

ABSTRACT: Intermediate glacial states were characterized by large temperature changes in Greenland and the North Atlantic, referred to as Dansgaard–Oeschger (D–O) variability, with some transitions occurring over a few decades. D–O variability included changes in the strength of the Atlantic meridional overturning circulation (AMOC), temperature changes of opposite sign and asynchronous timing in each hemisphere, shifts in the mean position of the Intertropical Convergence Zone and variations in atmospheric CO_2. Palaeorecords and numerical studies indicate that the AMOC, with a tight coupling to Nordic Seas sea ice, is central to D–O variability, yet, a complete theory remains elusive. In this Review, we synthesize the climatic expression and processes proposed to explain D–O cyclicity. What emerges is an oscillatory framework of the AMOC–sea-ice system, arising through feedbacks involving the atmosphere, cryosphere and the Earth's biogeochemical system. Palaeoclimate observations indicate that the AMOC might be

more sensitive to perturbations than climate models currently suggest. Tighter constraints on AMOC stability are, thus, needed to project AMOC changes over the coming century as a response to anthropogenic carbon emissions. Progress can be achieved by additional observational constraints and numerical simulations performed with coupled climate–ice-sheet models.

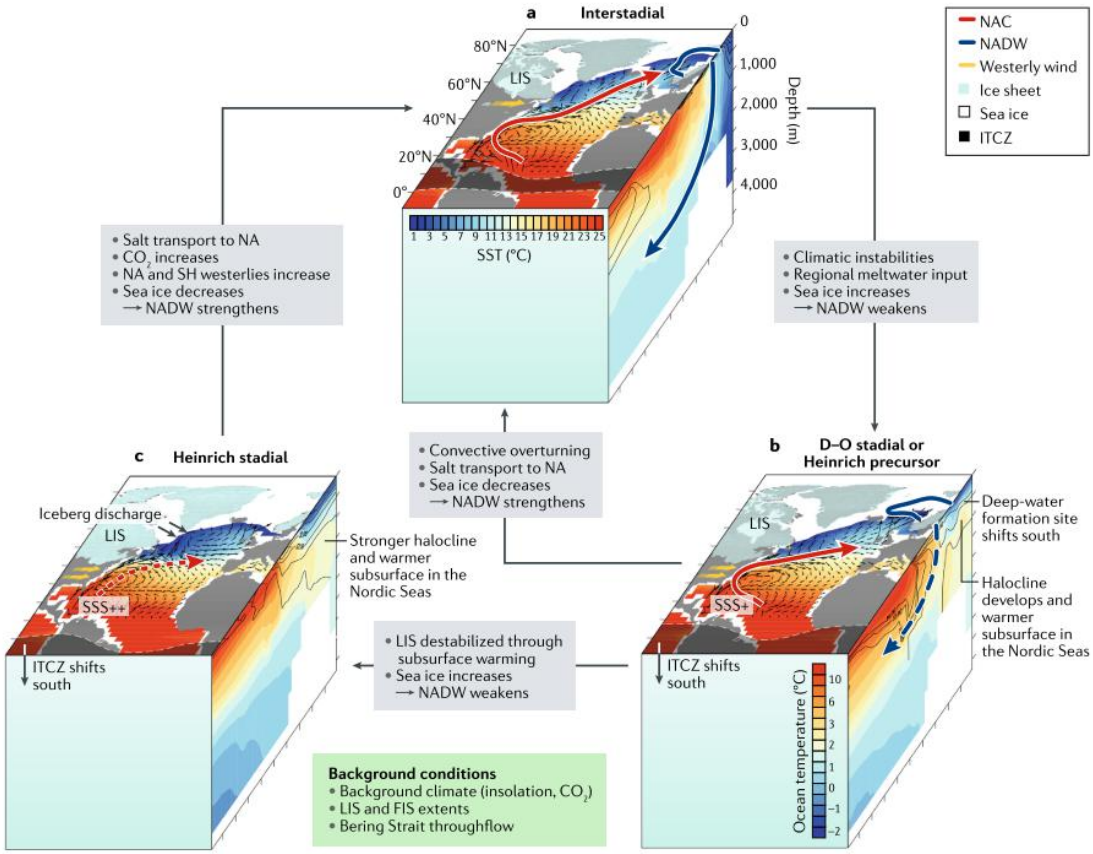

Figure 1. Summary of interactions and feedbacks involved in D–O variability. Schematic of an interstadial peak (panel a), a Dansgaard– Oeschger (D–O) stadial or Heinrich precursor (panel b) and a Heinrich stadial (panel c) showing the possible mechanisms leading to transitions. These schematics qualitatively illustrate the main climatic changes associated with D–O variability, taking into account the large uncertainties associated with quantitative estimates. On going from interstadials to D–O and Heinrich stadials, North Atlantic Deep Water (NADW) formation weakens, deep- water formation sites shift southward, sea- ice extent increases, the annual mean sea- surface temperature (SST) decreases and surface currents (black arrows) are modified, with, in particular, weakening of the North Atlantic Current (NAC). The subsurface temperature in the northern North Atlantic (NA) increases (the side panel shows the annual mean zonally averaged temperature in the Atlantic with respect to depth and

latitude), while a stronger halocline develops (side panel contours). Warmer subsurface conditions could destabilize the Laurentide Ice Sheet (LIS) and lead to iceberg discharges in the Hudson Strait, which is characteristic of Heinrich events. As the Atlantic meridional overturning circulation (AMOC) weakens, the Intertropical Convergence Zone (ITCZ) shifts southward, increasing sea- surface salinity in the tropical Atlantic (SSS+). A possible southward extension of the LIS during stadials would intensify North Atlantic westerly winds (yellow arrows). Breakdown of the halocline through convective overturning or increased salt transport to the North Atlantic could lead to a stadial to interstadial transition. Stronger Northern Hemisphere westerlies (arising from LIS changes), Southern Hemisphere (SH) westerlies or increased atmospheric CO2 concentration during Heinrich stadials could also contribute to AMOC reinvigoration towards an interstadial. Favourable background conditions for D–O variability to occur are indicated in green. FIS, Fennoscandian Ice Sheet.

11. 亚南极乔治亚南部冰原泥炭对晚全新世气候与冰川变化的响应

翻译人：李海 12031330@mail.sustech.edu.cn

Xia Z, Oppedal L T, Van der Putten N, et al. ***Ecological response of a glacier-fed peatland to late Holocene climate and glacier changes on subantarctic South Georgia*** *[J]. Quaternary Science Reviews, 2020, 250: 106679.*

https://doi.org/10.1016/j.quascirev.2020.106679

摘要: 冰原泥炭地沉积物提供了过去冰川变化的记录，但对形成这些泥炭生态系统的动力学研究较少。对一个 204 cm 深的泥炭钻孔沉积物进行多参数的研究，重建了 4300 年以来亚南极乔治亚南部冰原泥炭对气候和冰川变化的生态响应。4300 - 2550 cal yr BP 间在区域地热气候及冰川较小的作用下，泥炭地稳定且保持快速的碳沉积和棕色苔藓与单子植物之间的动态更新。碳沉积速率在气候变暖的驱动下在 4000–3500 cal yr BP 和 3200–2700 cal yr BP 间出现两个高峰期，峰值分别为 140 g C m^{-2} yr^{-1} 和 70 g C m^{-2} yr^{-1}。棕色苔藓纤维素的$\delta^{13}C$ 和 $\delta^{18}O$ 的结果显示，冰川融水对泥炭地植被造成短期干扰，表明暖期冰川融水仍能影响泥炭地生态系统。2550 cal yr BP 以来，由于冷却驱动的冰川推进改变了侵蚀和融水机制，增加了冰川沉积物流入泥炭地，以苔藓为主的植被遭破坏，泥炭碳沉积速率下降到 15 g C m^{-2} yr^{-1}。尽管这种融水扰动增强机制自过渡期以来一直持续，但在 1200-600 cal yr BP 的中世纪气候变暖期，棕色苔藓栖息地逐渐恢复，并在此后成为主导。棕色苔藓的重建可能得益于碳沉积速率的增加，在 1200-900 cal yr BP 的碳沉积速率达到 100 g C m^{-2} yr^{-1}，从而建立了有机质基质并稳定了栖息地。研究表明，区域气候和冰川活动的相互作用对冰期泥炭地的生态系统动力学具有重要影响。该研究也显示了稳定同位素分析在研究非泥炭地古水文中的潜力。

Abstract: Sedimentary deposits from glacier-fed peatlands provide records of past glacier variability, but the dynamics of these peat-forming ecosystems have rarely been investigated. Through multi-proxy analyses of a 204-cm peat core, we reconstructed the ecological response of a glacier-fed peatland on subantarctic South Georgia to climate and glacier variability over the last 4300 years. A stable peatland with rapid carbon accumulations and dynamic turnovers between brown mosses and monocots persisted between 4300 and 2550 cal yr BP when the up-valley cirque glacier was small under a regional hypsithermal climate. Carbon accumulation rates showed two peak periods driven by climate warming, reaching 140 g C m^{-2} yr^{-1} at 4000–3500 cal

yr BP and 70 g C m^{-2} yr^{-1} at 3200–2700 cal yr BP. Paired $\delta^{13}C$ and $\delta^{18}O$ data from brown moss cellulose reveal several intervals of glacial meltwater inundation that caused short-term disturbances of the peatland vegetation, indicating that glacial meltwater potentially still affected the peatland ecosystem during this warm period. Moss-dominated vegetation was disrupted and peatland carbon accumulation rates decreased to 15 g C m^{-2} yr^{-1} after around 2550 cal yr BP when a cooling-driven glacier advance shifted the erosion and meltwater regime enhancing the glacial sediment influx onto the peatland. Although this enhanced regime of meltwater disturbance has continued since this transition, the brown moss habitat was gradually re-established during the medieval climate warming between 1200 and 600 cal yr BP and then became dominant shortly after that. This re-establishment of brown mosses might have benefited from a period of increased carbon accumulation rates up to 100 g C m^{-2} yr^{-1} at 1200–900 cal yr BP that built up the organic matter matrix and stabilized the habitat. We conclude that the ecosystem dynamics of glacier-fed peatlands is strongly shaped by the interplay between regional climate and glacier activity. This study also demonstrates the potential of stable isotope analysis in studying the paleohydrology of non-Sphagnum peatlands.

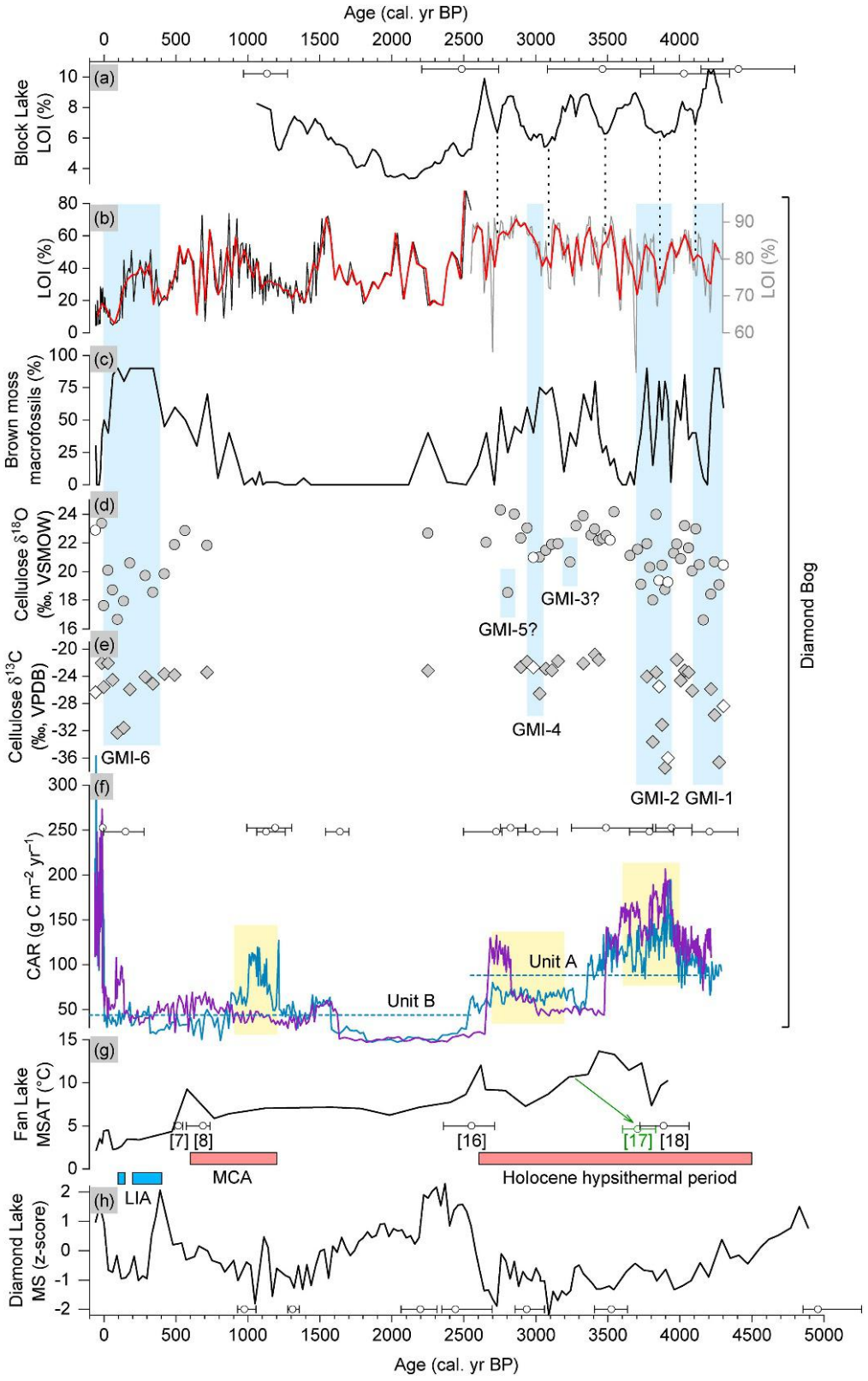

Figure 1. Summary of proxy data from the DB2 peat core (plotted on the Bacon age-depth model) and comparisons with other regional records. For all these records, their radiocarbon dating points are also shown as dots with error bars (calibrated calendar median age with 2σ error). The calendar age is

relative to 1950 CE. (a) Block Lake LOI data (5% running mean) (Rosqvist and Schuber, 2003) plotted on an updated age-depth model. (b) DB2 LOI data plotted on different vertical scales for Unit A (right vertical axis; gray line) and Unit B (left vertical axis; back line) and their 30-year bin values (red lines). The dotted lines connect the corresponding low LOI values in (a) and (b) despite a less certain chronology for the Block Lake record. (c) DB2 brown moss macrofossil percentage. (d) DB2 brown moss cellulose δ18O. (e) DB2 brown moss cellulose δ13C. In (d) and (e), gray and white symbols represent the data points from Warnstorfia sp. and Sanionia sp. macrofossils, respectively. The light blue vertical bands indicate six inferred glacial meltwater inundation (GMI) intervals. (f) DB2 "instantaneous" CARs plotted on the Bacon age-depth model (dark blue line) and the Clam age-depth model of linear interpolation (purple line). Also shown are the time-weighted mean CARs for Units A and B (dark blue horizontal dashed line) based on the Bacon age-depth model. The yellow bands indicate the observed peaks in CARs. (g) Mean summer air temperature (MSAT) record reconstructed from Fan Lake (Foster et al., 2016). Here the chronological anchor points for these temperature peaks used by Strother et al. (2015) are also shown along with their ID numbers (7, 8, 16, and 18). The green radiocarbon dating point (ID number 17) was rejected in the original age-depth model, but if used, the horizon of 3250 cal yr BP would be anchored to an older age, pulling this section of the MSAT curve rightward in the Bayesian age-depth modeling. The red horizontal bars below show the periods of past warm intervals by Foster et al. (2016) based on their multi-proxy dataset. MCA–Medieval Climate Anomaly. (h) Diamond Lake bulk magnetic susceptibility record that was used to reconstruct the size of Diamond Glacier, with a higher value indicating a larger glacier (Oppedal et al., 2018a). The blue horizontal bars above show the interval of Little Ice Age (LIA), including the peak stage at 380–220 cal yr BP and the second stage at 120 cal yr BP, defined from a well-dated high-resolution glacier-fed lake sediment record at nearby the Hamberg catchment by van der Bilt et al. (2017) (south of Fig. 1c area). (For interpretation of the references to colour in this figure legend, the reader is referred to the Web version of this article.)

12. 澳大利亚板块 Woyla 弧（印度尼西亚、苏门答腊）早白垩世起源

翻译人：周洋 zhouy3@sustech.edu.cn

Advokaat E L, Bongers M LM, Rudyawan A, et al. ***Early Cretaceous origin of the Woyla Arc (Sumatra, Indonesia) on the Australian plate*** *[J]. Earth and Planetary Science Letters, 2018, 498: 348–361.*

https://doi.org/10.1016/j.epsl.2018.07.001.

摘要：新特提斯洋其南部为来自冈瓦纳大陆的印度板块和澳大利亚板块，北部为欧亚大陆。要了解新特提斯洋板块运动演化的关键就是要重建现在完全被俯冲掉的板块。这些大洋板块遗迹以蛇绿岩和岛弧的形式存在，增生的造山带从喜马拉雅山脉延伸至东南亚，直至巽它大陆南缘。洋内弧 Woyla 弧在白垩纪中期仰冲至巽它大陆之上。以前 Woyla 弧被认为于早白垩世在西向俯冲带上方形成，与巽它大陆之下的东向俯冲同步。Woyla 弧和巽它大陆之间的大洋板块‘Ngalau Plate’因俯冲而消失。我们对来自 Woyla 弧的下白垩统灰岩和火山碎屑岩，Ngalau 板块的中侏罗世含放射虫硅质岩和巽它大陆边缘的上侏罗统-下白垩统碎屑沉积进行了古地磁测试。结果表明，Woyla 弧是在赤道纬度附近形成，并且仅相对于巽它大陆发生了向东的运动。这与在澳大利亚板块边缘形成 Woyla 弧的情况是一致的。据此我们提出了一个重建方案，其中在 N—S 走向的 Woyla 弧和 NW—SE 走向的巽它大陆之间形成了一个三角形洋盆（Ngalau 板块），以解释喜马拉雅山脉中不存在增生的岛弧岩石。由于这种三角形的几何形状，Woyla 弧向巽它大陆西部边缘的增生是不等时的。澳大利亚与欧亚大陆的持续汇合由 Woyla 弧俯冲极性反转所调节，这可能被印度-缅甸山脉和安达曼-尼科巴群岛的白垩纪蛇绿岩所记录。

ABSTRACT: Key to understanding the plate kinematic evolution of the Neotethys oceanic domain that existed between the Gondwana-derived Indian and Australian continents in the south, and Eurasia in the north, is the reconstruction of oceanic plates that are now entirely lost to subduction. Relics of these oceanic plates exist in the form of ophiolites and island arcs accreted to the orogen that stretches from Tibet and the Himalayas to SE Asia that formed the southern

margin of Sundaland. The intra-oceanic Woyla Arc thrusted over western Sundaland – the Eurasian core of SE Asia – in the mid-Cretaceous. The Woyla Arc was previously interpreted to have formed above a west-dipping subduction zone in the Early Cretaceous, synchronous with east-dipping subduction below Sundaland. The oceanic 'Ngalau Plate' between the Woyla Arc and Sundaland was lost to subduction. We present paleomagnetic results from Lower Cretaceous limestones and volcaniclastic rocks of the Woyla Arc, Middle Jurassic radiolarian cherts of the intervening Ngalau Plate, and Upper Jurassic–Lower Cretaceous detrital sediments of the Sundaland margin. Our results suggest that the Woyla Arc was formed around equatorial latitudes and only underwent an eastward longitudinal motion relative to Sundaland. This is consistent with a scenario where the Woyla Arc was formed on the edge of the Australian plate. We propose a reconstruction where the Ngalau Plate formed a triangular oceanic basin between the N–S trending Woyla Arc and the NWSE trending Sundaland margin to account for the absence of accreted arc rocks in the Himalayas. As consequence of this triangular geometry, accretion of the Woyla Arc to the western Sundaland margin was diachronous, accommodated by a southward migrating triple junction. Continuing convergence of the Australia relative to Eurasia was accommodated by subduction polarity reversal behind the Woyla Arc, possibly recorded by Cretaceous ophiolites in the Indo-Burman Ranges and the Andaman-Nicobar Islands.

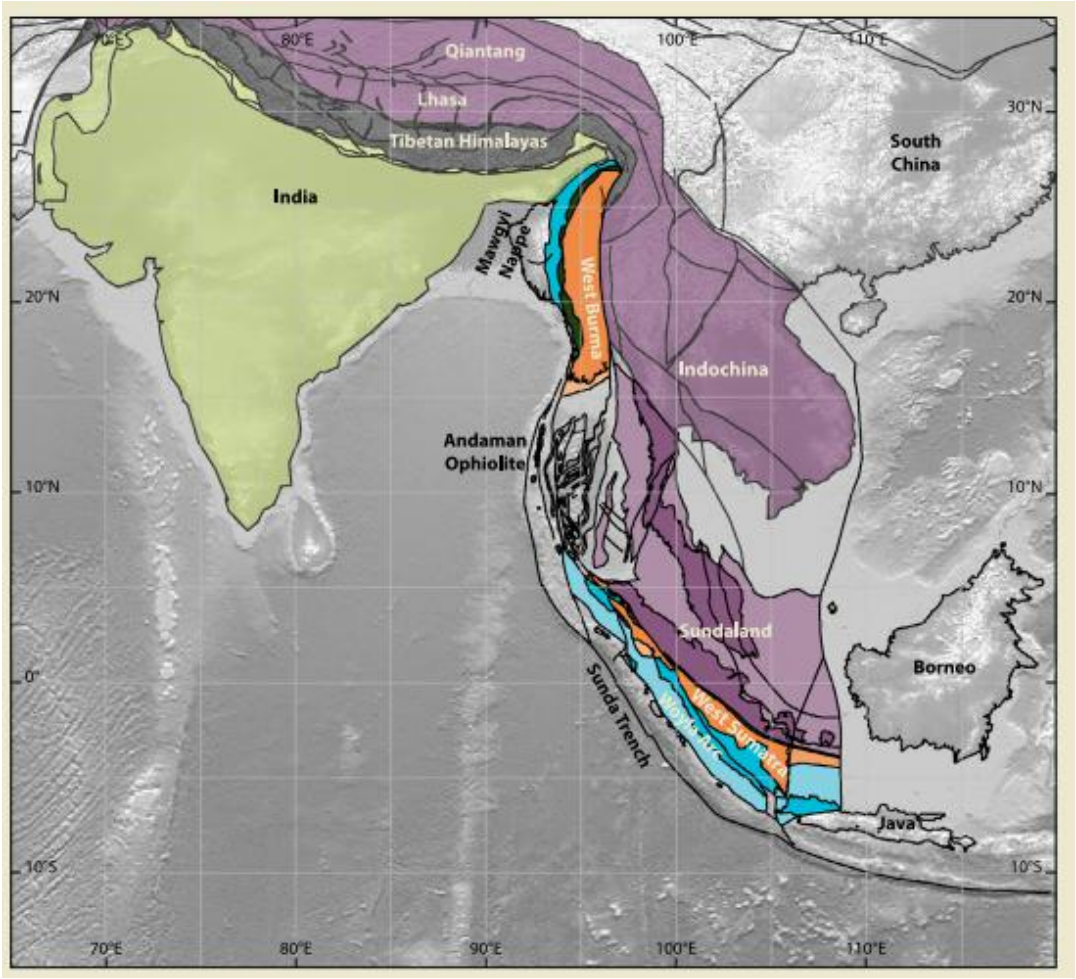

Figure 1. Map of continental and arc fragments in SE Asia

13. 来自非洲-阿拉伯大火成岩省 Ethiopia 地区 Lima-Limo 剖面约 30Ma 的地磁场古强度结果

翻译人：张伟杰 12031188@mail.sustech.edu.cn

Yoshimura Y, Yamazaki T, Yamamoto Y, et al. ***Geomagnetic paleointensity around 30 Ma estimated from Afro-Arabian Large Igneous Province in Lima-Limo section, Ethiopia*** *[J]. Geochemistry, Geophysics, Geosystems. 2020.*

https://doi.org/10.1029/2020GC009341

摘要：我们对分布在非洲-阿拉伯大火成岩省 Lima-Limo 剖面分布的约 30Ma 的熔岩流进行了地磁场古强度研究。对来自 45 个熔岩流的 120 块样品进行包含低温退磁与双加热过程的 Tsunakawa-Shaw 方法实验，成功地从 34 个熔岩流 75 块样品中获得了古强度结果。我们测量了磁滞回线与热磁曲线去检验磁学性质对古强度的影响，但是没有发现古强度结果与磁滞参数比值之间具有相关性。基于热磁曲线结果我们排除了可能包含钛磁赤铁矿的样品，然后计算了 27 个熔岩流各自古强度的平均值。我们观察到在最下部反极性带古强度值呈周期性变化，这反映了地磁场的长期变化。为了去评估~ 30Ma 代表性的虚轴向偶极矩（VAMD），我们进行了依赖于样品数的熔岩流选择。11 个熔岩流通过了选择标准，得到的平均 VADM 为 4.2 ± 2.1 × 1022 Am^2。这个结果与之前报道的晚白垩世与新生代的 5 个使用 Tsunakawa-Shaw 方法得到的结果相似。综合了 25~35Ma 可利用的数据，我们认为通过 32 个熔岩流平均得到的 4.4 × 1022 Am^2，代表了这一时期的古地磁场强度。这个结果接近于 2 个之前报道的从侏罗纪开始的长期代表性的 V(A)DMs。

ABSTRACT: We conducted a geomagnetic paleointensity study of lava flows at ~ 30 Ma distributed in the Lima-Limo section of the Afro-Arabian Large Igneous Province. The Tsunakawa-Shaw method, which has built-in low-temperature demagnetization and double heating procedures, was applied to 120 specimens from 45 lava flows, successfully obtaining paleointensities from 75 specimens within 34 lava flows. We measured hysteresis loops and thermomagnetic curves to examine the influence of magnetic properties on the paleointensities but found no relationship between the paleointensities and the ratios of the hysteresis parameters. We

calculated 27 flow-level paleointensity means after excluding specimens that possibly contain titanomaghemite based on thermomagnetic curves. We observed cyclic changes of paleointensity in the lowest reversed magnetozone, which may reflect paleosecular variations. To estimate a representative virtual (axial) dipole moment (V(A)DM) at ~ 30 Ma, we applied a flow-level selection criterion depending on the specimen numbers. Eleven flow-level means passed the criterion, which gave an averaged VADM of $4.2 \pm 2.1 \times 10^{22}$ Am^2. This is similar to five averaged V(A)DMs reported previously in the Late Cretaceous and the Cenozoic using the Tsunakawa-Shaw method. We combined our data with available data between 25 and 35 Ma. We concluded that the mode of 4.4×10^{22} Am^2 from 32 flow-level means is representative of this period. This is close to two previously reported long-term representative V(A)DMs since the Jurassic.

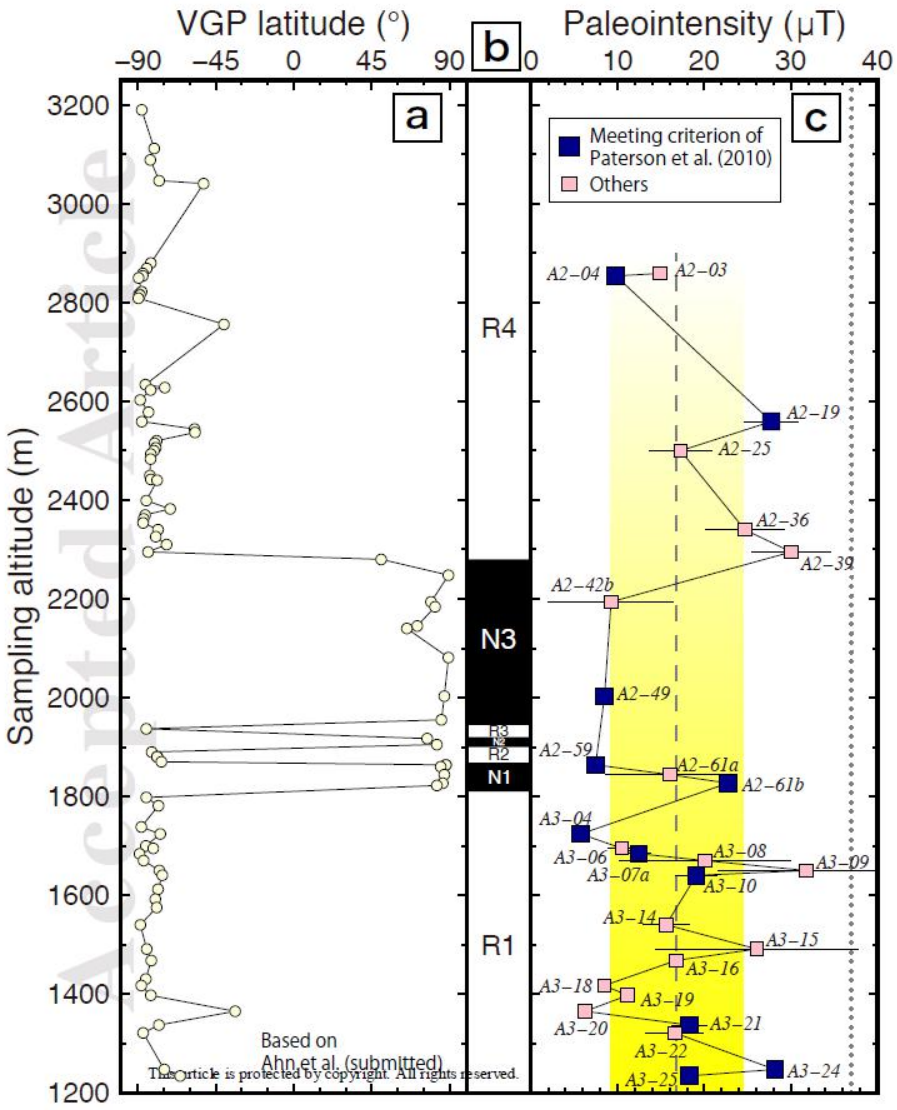

Figure 1. (a) VGP latitudes of individual lava flows in the Lima-Limo section of AALIP, which are based on Ahn et al. (2020) and corrected for African plate motion. (b) Magnetozones recognized by Ahn et al. (2020). (c) Flow-level means of paleointensities. Error bars are standard deviations. Dark blue squares represent acceptable data passing the consistency criterion of Paterson et al. (2010), while pink squares are other data. The dashed gray line and yellow zoneare the averaged paleointensity of all flow-level means (not selected) and its standard deviation. The dotted gray line indicates the present field strength at the Lima-Limo section (IGRF-13).

14. 环境因素在海洋生物泵长期演化中的作用

翻译人：张亚南 zhangyn3@mail.sustech.edu.cn

Fakhrae M, Planavsky N J, Reinhard C T. ***The role of environmental factors in the long-term evolution of the marine biological pump*** *[J]. Nature Geoscience, 2020, 13: 812-816.*

https://doi.org/10.1038/s41561-020-00660-6

摘要：生物泵作为将大气 CO_2 转化成有机质输送到海洋内部和沉积物中的传输器，在调节长时间尺度碳循环、大气组成和气候方面扮演着重要的角色。尽管其在地球系统中十分关键，但在地球历史的大部分阶段，生物泵对生物革新和气候波动的反应都是猜测的。我们通过生物泵的机理模型重新审视了控制碳传输效率的影响因素。我们证明了从以细菌浮游生物为主到真核细胞更丰富的生态系统转变，不太可能对地球生物泵的效率造成很大的影响。相比之下，大型浮游动物在水体中垂直运动能力的进化，会加强碳元素在海洋内部的转移。但与环境驱动因素相比，浮游动物对生物泵的影响仍然相对较小。特别是海洋温度的升高和大气氧含量的增加导致全球有机碳输送效率的显著降低。综上所述，我们的研究结果对藻类多样性与地球氧化之间的因果关系提出了质疑，并表明地球历史上的气候扰动在推动海洋内部碳固定和地球表层氧化方面发挥了重要的作用，但还未被重视。

ABSTRACT: The biological pump—the transfer of atmospheric carbon dioxide to the ocean interior and marine sediments as organic carbon—plays a critical role in regulating the long-term carbon cycle, atmospheric composition and climate. Despite its centrality in the Earth system, the response of the biological pump to biotic innovation and climatic fluctuations through most stages of Earth's history has been largely conjectural. Here we use a mechanistic model of the biological carbon pump to revisit the factors controlling the transfer efficiency of carbon from surface waters to the ocean interior and marine sediments. We demonstrate that a shift from bacterioplankton-dominated to more eukaryote-rich ecosystems is unlikely to have considerably impacted the efficiency of Earth's biological pump. In contrast, the evolution of large zooplankton capable of vertical movement in the water column would have enhanced carbon transfer into the

ocean interior. However, the impact of zooplankton on the biological carbon pump is still relatively minor when compared with environmental drivers. In particular, increased ocean temperatures and greater atmospheric oxygen abundance lead to notable decreases in global organic carbon transfer efficiency. Taken together, our results call into question causative links between algal diversification and planetary oxygenation and suggest that climate perturbations in Earth's history have played an important and underappreciated role in driving both carbon sequestration in the ocean interior and Earth surface oxygenation.

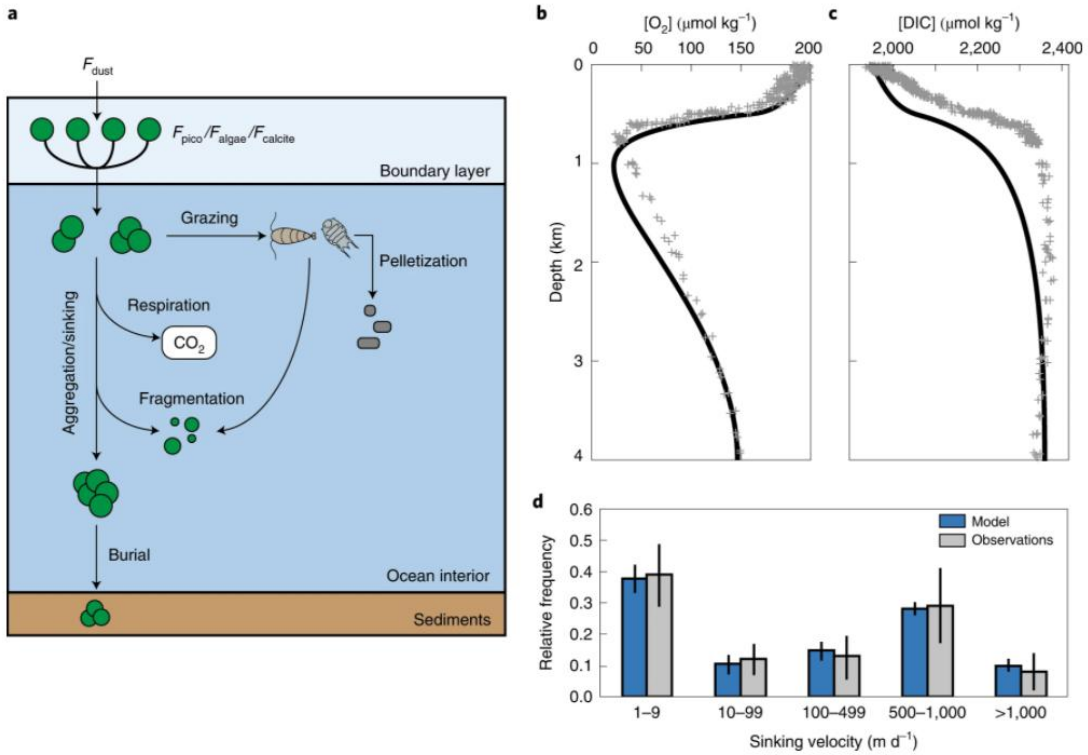

Figure 1. Schematic of the mechanistic model of the ocean biological carbon pump. a, The major processes controlling the transfer efficiency of organic carbon in marine sediments (Supplementary Information). F_{dust}, F_{pico}, F_{algae} and $F_{calcite}$ represent imposed relative fluxes of windblown dust, picoplankton, eukaryotic algae, and calcite, respectively, in primary particles. b–d, Comparison of results from our modern model configuration (black curves) with observational water column data from the North Pacific Ocean (grey crosses) for concentration of dissolved oxygen ([O_2]; b) and dissolved inorganic carbon ([DIC]; c) together with validation of model results against observations of the size–velocity spectrum of marine aggregates in the modern oceans (d). Error bars in d denote one standard deviation.

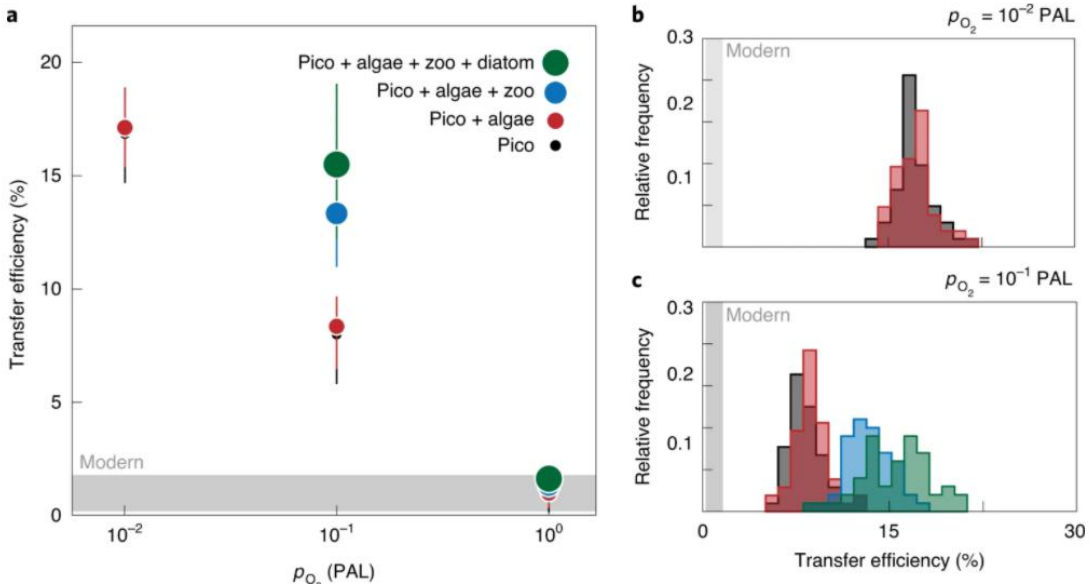

Figure 2. The impact of first-order changes to plankton ecology on the ocean biological carbon pump. Values of transfer efficiency are calculated using the oxic and anoxic power laws and without temperature dependency on organic carbon remineralization ($Q_{10} = 1$). a, Net organic carbon transfer efficiencies as a function of atmospheric p_{O2} relative to PAL and across a range of ecological scenarios: (1) default Precambrian scenario with picoplankton, no algae and high dust flux due to lack of land plants (pico; black); (2) a late Proterozoic scenario, similar to (1) but with a small contribution of algae to ocean productivity (pico+algae; red); (3) an early Phanerozoic scenario, with faecal pellet production by zooplankton and increased contribution of algae (pico+algae+zoo; blue); and (4) a late Phanerozoic scenario with more complex eukaryotic algae (including diatoms) and an attenuated dust flux promoted by the emergence of vascular planets in terrestrial ecosystems (pico+algae+zoo+diatom; green). Error bars show the 90% credible interval from a Monte Carlo analysis of model parameters (Supplementary Information). b,c, Resampled distributions at two discrete atmospheric p_{O2} values, with colours corresponding to the scenarios shown in a. Modern open-ocean organic carbon transfer efficiencies are shown in all panels by grey shaded boxes.

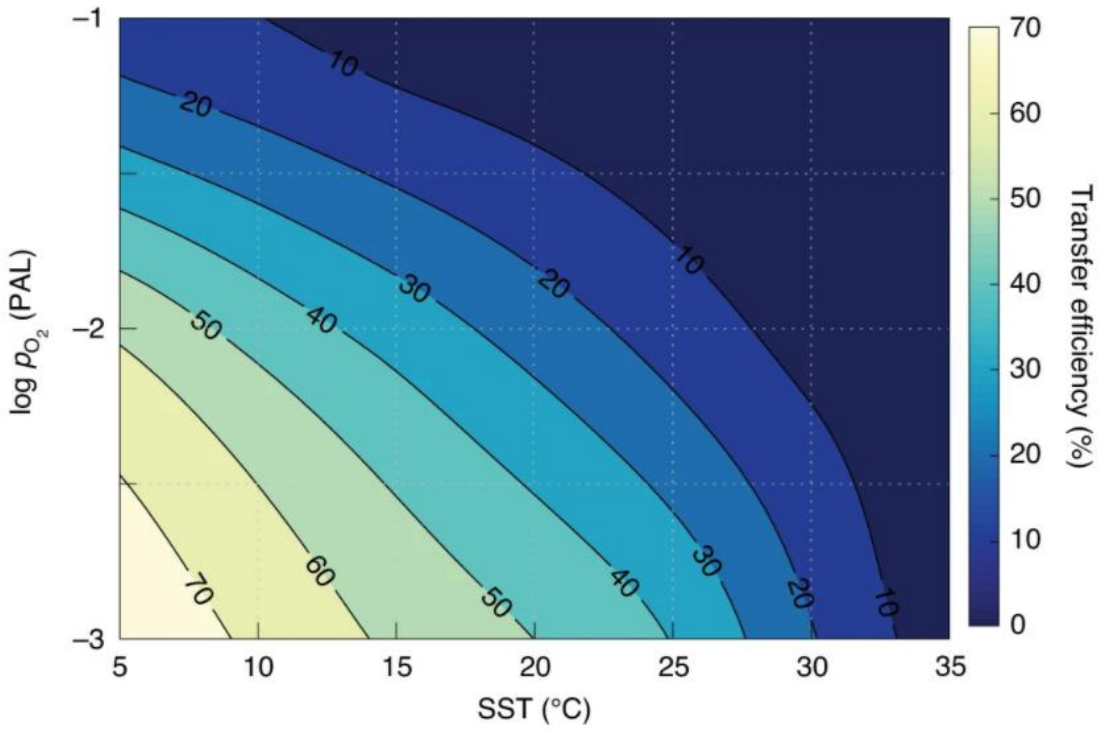

Figure 3. The impact of ocean temperature and atmospheric oxygen abundance on the ocean biological carbon pump. Temperatures are reported as sea surface temperature (SST), while atmospheric p_{O2} is given relative to PAL. Note the log scale for atmospheric p_{O2}. Organic carbon transfer efficiency (%) is calculated as the fraction of carbon exported from the surface ocean that is delivered to the sediment–water interface.